CARMEN: Center for Automated Vehicle Research with Multimodal Assured Navigation A

USDOT Tier-1 University Transportation Center

Experimentation, Demonstration and Testing of PNT Related Threats, Risks, and Mitigations to HATS

Charles Toth (https://orcid.org/0000-0001-9461-4887)
Todd Humphreys (https://orcid.org/0000-0003-0749-6988)

FINAL RESEARCH REPORT – November 30, 2023

Contract # 69A3552047138

Acronyms

AIC	Akaike Information Criterion
CDGNSS	Carrier-phase Differential GNSS
GNSS	Global Navigation Satellite System
GPS	Global Positioning System
HATS	Highly Automated Transportation System
IMU	Inertial Measurement Unit
LiDAR	Light Detection and Ranging
MBS	Metropolitan Beacon System
NIS	Normalized Innovation Squared
OLS	Ordinary Least Squares
PNT	Positioning, Navigation and Timing
PVT	Positioning, Velocity and Timing
SDR	Software Defined Receiver
SLAM	Simultaneous Localization And Mapping
TRNS	Terrestrial Radionavigation System
UAM	Urban Air Mobility
UAS	Unmanned/Uncrewed Airborne System
UWB	Ultra-wide Band
V2I	Vehicle to Infrastructure
V2V	Vehicle to Vehicle
V2X	Vehicle to Everything
WLS	Weighted Least Squares

Abstract

The integrity of a PNT system can be monitored at three primary levels. The first one is the GPS/GNSS system level, which includes the signal structure/authentication and signal power/diversity which is beyond the scope from a user perspective. The second, the GPS/GNSS receiver level is of high interest and techniques include antenna design, receiver integrity monitoring (RAIM/ARAIM), other algorithms to handle various integrity events. The third level, the PNT system level, which is primarily about sensor integration; mainly, considering non-RF sensors. The classical GNSS/IMU integration is the very foundation of most navigation systems, which has been gradually extended to incorporate data from other sensors, such as optical imagery (vision), LiDAR, Radar, etc. These environment-based approaches provide observations of natural and man-made structures. For example, surface undulation, texture, buildings, roads, etc., can be used to both local and global navigation. Similarly, the magnetic field or gravity of the Earth, and then infrastructures that are not designed for navigation can also provide data that can support both relative and absolute navigation. In this study, the focus is on some specific cases of the second and third monitoring levels; in particular, some new approaches applicable to the third level.

Until now the integrity monitoring, to identify natural and human induced threats to a PNT system has been addressed from a GNSS receiver or single platform PNT perspective. In other words, collecting all the data provided by sensors deployed on the platform, a sensor integration solution attempts to obtain the optimal navigation solution as well as to detect any anomalies that could impact the trust in the navigation solution. Since platforms hardly operate alone, just think about the congestion on road or crowds gathering at certain events or air spaces filled up with UAS, there is an opportunity to exploit the geometrical relationship of the platforms and thus to achieve a better navigation solution for all the platforms and additionally harness the opportunity to detect threats to the PNT solution. To investigate the potential of collaborative navigation, a major dataset was acquired in a simulated intersection area, where multiple vehicles, cyclists, pedestrians and UAS platforms simultaneously operated. This dataset provides essential data to simulate various threat scenarios on real data as well as to benchmark the performance of emerging methods. Sensors can be subjected to systematic denial (i.e., jamming) and deception (i.e., spoofing) attacks, starting with individual sensor attacks and ending in cross-sensor coordinated attacks, to evaluate the resilience of the PNT sensing platform and its underlying algorithms to deliberate malfeasance.

Contents

List of Figures

List of Tables

1 Introduction

The investigation of various PNT threat and issues have relied on both simulated data as well as field data collected on actual traffic intersection setup at West Campus of the Ohio State University. Researchers used multiple vehicles equipped with sensing, including GPS/GNSS, IMU, LiDAR, and camera, and communication equipment, including UWB and local WiFi networks. At the selected test locations, data was acquired for several scenarios, and constituted the basis for assessing risks and vulnerabilities to an assortment of modes, and transportation contexts, and potential mitigation possibilities.

A unique aspect of the main data acquisition campaign in May 2022 was to acquire multi-modal data in the simulated intersection area. Ground vehicles, pedestrians and cyclists moved in the area while several UAS flew above them. This arrangement provided to extend the observation space from 2D to 3D, and thus, allowing to assess the challenges and benefits of the different platforms cooperating on the ground and in the air separately as well as jointly in the space. From a theoretical perspective, the platforms formed 2D and/or 3D geodetic networks, and the network geometry could be exploited to both improve joint navigation of the platforms and detect, and potentially mitigate, anomalies applied to either the GPS receiver or the entire PNT system.

All the four ground vehicles, two cyclists, two pedestrians and the four UAS were equipped with GPS/GNSS receivers to provide accurate reference trajectories that were essential for performance evaluations. Then, IMUs, cameras, LiDAR sensors, UWB transceivers, smartphones, etc., were installed on the platforms in various configurations, which were primarily controlled by the availability of the sensors. In addition, a static network was installed at the simulated intersection area to allow communication and platform positioning based on typical road infrastructure. In addition, these reference locations were outfitted with visible targets allowing for image-based positioning and referencing primarily from air but also from the ground vehicles. During the one-week data acquisition campaign, multiple scenarios were considered, in terms of number of platforms participating or the motion pattern of the platforms, etc. The various data streams be subjected to systematic denial (i.e., jamming) and deception (i.e., spoofing) attacks, starting with individual sensor attacks and ending in cross-sensor coordinated attacks, to evaluate the resilience of the PNT sensing platform and its underlying algorithms to deliberate malfeasance. The entire dataset with the benchmark trajectory data is publicly available on GitHub.

Another important dataset was acquired in the Bay Area by The University of Texas at Austin Radionavigation Laboratory. The focus was to provide representative data in urban environment to jointly assess GNSS and TRNS systems with respect to achieving assured navigation to support UAM. A UAS platform equipped with GNSS and TRNS receivers, IMU, camera, Radar and barometer acquired data.

2 Analysis, Simulation, and Experimental Demonstration and Testing of PNT Threat Scenarios and Risks

Field experiments and demonstrations conducted to simulate PNT threats and scenarios are reported in this section. This activity was originally reported in [1-6].

2.1 Field Data Collection and Demonstration

A massive field test, including multiple ground and UAS platforms was organized and executed on OSU West Campus, May 8-16, 2022 (Suleymanoglu *et al.,* 2023). The main objective was to acquire test data to support research on GNSS and PNT system operational anomaly detection using collaborative navigation as well as to support other UTC research efforts to simulate threat and risk scenarios based on real data. The ground platforms included four vehicles, two cyclists and two pedestrians, and then four simultaneously flying UAS in the air. At the peak of experiments, the number of directly involved people was 22, including faculty, students, and staff. The photo of the core participants of the ground data collection with the OSU CyberCar is shown in Figure 1

Figure 1 The team of ground platform-based data acquisition with the OSU CyberCar.

The data collection over eight days included deployment and surveying of ground targets, setting up an UWB network, ground vehicle data collection sessions, UAS rehearsal flights, and combined ground/air data acquisitions and a few repeat tests. The ground platforms and drones primarily moved/flew predefined trajectories and rich sensor data was collected. There was no intention to use collaborative navigation software in real-time due to lack of communication capabilities, and thus, everything was logged for postprocessing.

A parking lot was selected for all these tests, suitable for multiple transportation modalities. The general pattern was to simulate traffic in a typical intersection area, where about 50% of traffic accidents happen. Figure 2 shows a remote parking lot of OSU West Campus from bird's eye view, which was practically unused by OSU during the tests and allowed to fly UAS without significant restrictions. Within the parking lot an area about of 50 m by 50 m was used for the main tests, where the central area of 30 m by 30 m was populated by signalized ground targets as well as UWB transceivers.

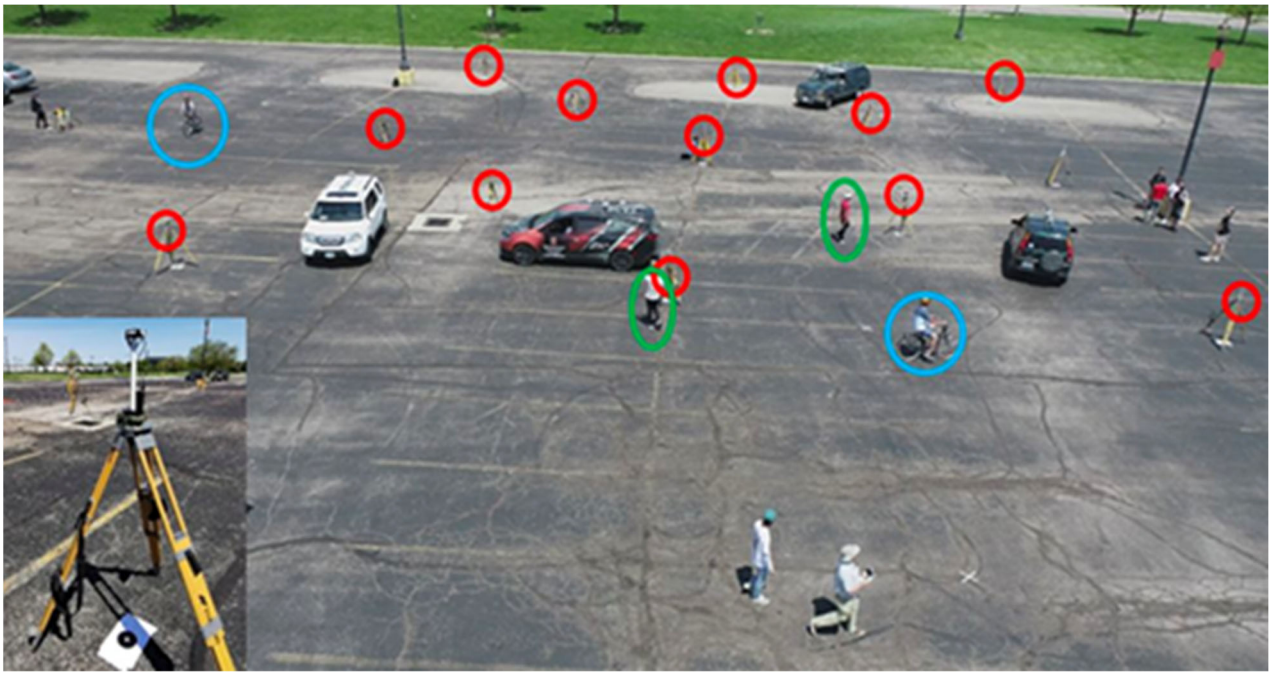

Figure 2 Field data acquisition using multiple platforms, including four vehicles, two cyclists marked by blue, two pedestrians marked by green, and 12 static UWB anchors mounted on tripods; insert shows ground target with UWB transceiver installed on tripod above.

During the data acquisition sessions, tripods were installed over the target locations and used to hold the UWB transceivers. The image-identifiable targets, see insert in Figure 2, provided ground control for imagery acquired from cameras mounted on UAS platforms and ground vehicles. The targets were surveyed with 1-2 cm horizontal and 2-3 cm vertical accuracy. In addition, the target locations were used to position 12 UWB

transceivers, forming the V2I network. Figure 3 shows the layout of the targets with the simulated lanes overlaid. The ranging measurements between the 12 nodes are shown with green lines, while the missing measurements, in particular, involving a 13th not properly working node, are marked in red.

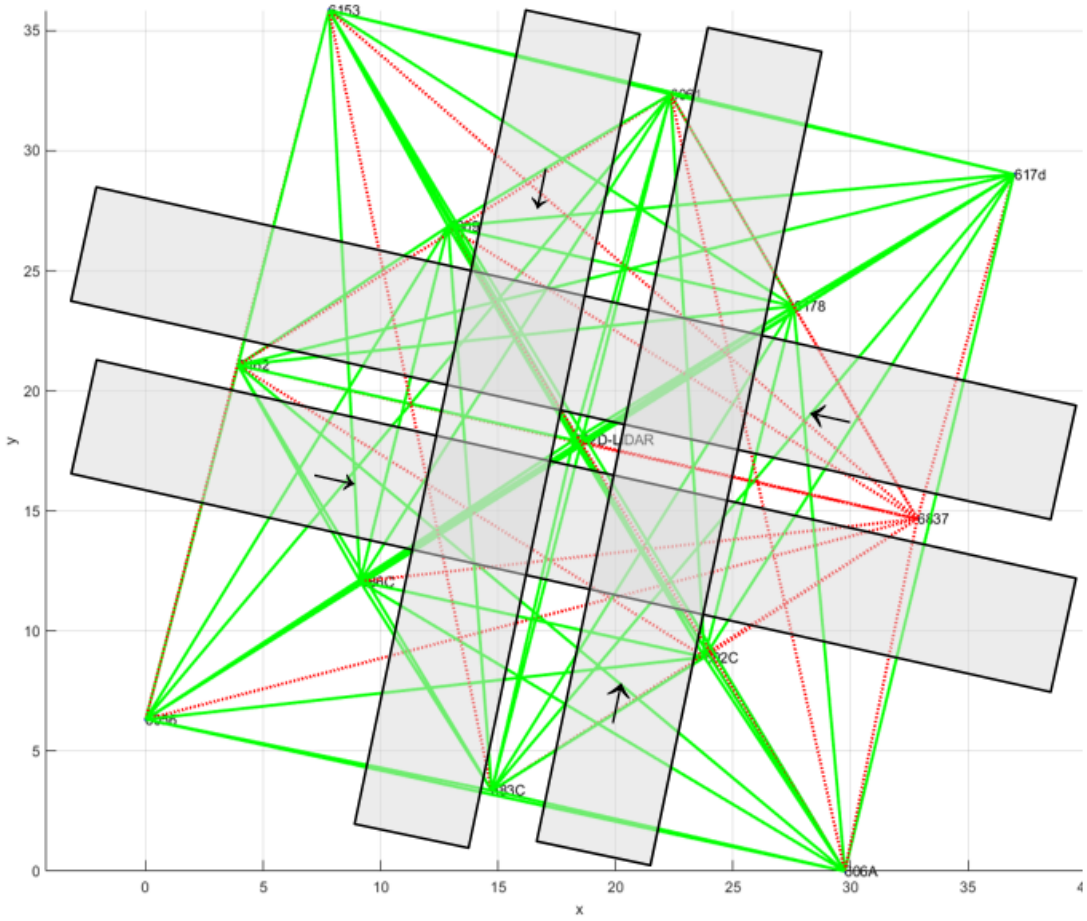

Figure 3 Target layout in the simulated intersection area with UWB V2I network.

Typical sensor configurations for the mobile ground platforms are shown in Figure 4. Most platforms had similar sensor setups, but the type of sensors varied due to the lack of availability of so many identical sensors. For example, the GNSS receivers were from four manufacturers or there were about ten different imaging sensors used.

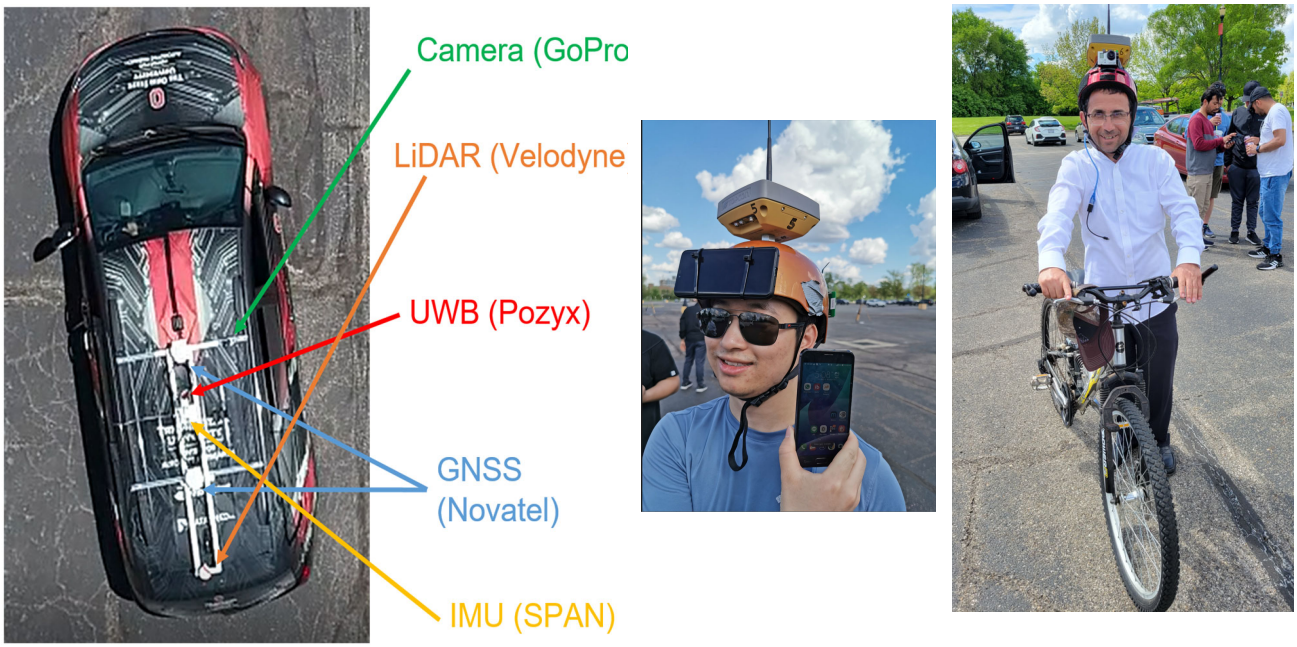

Figure 4 Typical sensor configuration on the three ground platforms.

2.2 Benchmark Dataset

To support research not only in the CARMEN project but for the larger research community in transportation and navigation area, we have created the *CONTEST* (Collaborative pOsitioning and NavigaTion bEtween ground and uaS plaTforms) dataset, aiming at providing multiple data streams to test collaborative positioning approaches, involving both terrestrial and aerial platforms, based on the use of several sensors, such as Ultra-Wide Band (UWB) transceivers, cameras, LiDARs, GNSS, etc. (Masiero et al., 2023).

Table 1 summarizes the platforms and sensors used during the data acquisition campaign and lists the data shared in the *CONTEST* dataset, which is available for download at the following link: https://github.com/3DOM-FBK/Collaborative_Navigation. Note that shared data have been created from raw data through some basic pre-processing and formatting operations, mostly aiming at improving the data usability.

Table 1 Summary of the platforms and sensors used during the data acquisition campaign, and the collected data streams that are shared in the CONTEST dataset (available at https://github.com/3DOM-FBK/Collaborative_Navigation).

Static Infrastructure	**Sensor**	**Data Acquired**	**Shared Data**
	12 UWB Pozyx (anchors)	-	reference positions
	LiDAR: Velodyne VLP16	raw profiles	raw profiles with timestamp
Platforms	**Onboard Sensor**	**Data Acquired**	**Shared Data**
UAS1 (DJI Phantom 4Pro RTK)	UWB: Pozyx	ranges	ranges wrt static and moving agents
	embedded GNSS	positions	reference trajectory
	embedded camera	images	images
UAS2 (DJI Phantom 4Pro)	UWB: Pozyx	ranges	ranges wrt static and moving agents
	GNSS: Emlid M2	positions	reference trajectory
	embedded camera	images	images
UAS3 (DJI Phantom 4Pro)	UWB: Pozyx	ranges	ranges wrt static and moving agents
	GNSS: Emlid M2	positions	reference trajectory
	embedded camera	images, videos	images, videos
UAS4 (DJI Matrice 210)	UWB: Pozyx	ranges	ranges wrt static and moving agents
	embedded GNSS	positions	reference trajectory
	Camera: DJI FC6310S	Images, videos	images, videos
Car 0 (GPSVan)	UWB: Pozyx	ranges	ranges wrt static and moving agents
	GNSS: Leica GS25, Septentrio PolRx5	positions	reference trajectory from GNSS and IMU integration and correction
	IMU: Honeywell H764G	inertial information	
	LiDAR Velodyne VLP16	raw profiles	raw profiles with timestamp
Car 1 (Honda CRV)	UWB: Pozyx	ranges	ranges wrt static and moving agents
	GNSS: Topcon HyperVR, Novatel PwrPak7	positions	reference trajectory from GNSS and IMU integration and correction
	IMU: SPAN-IGM-S1	inertial information	
	LiDAR Velodyne VLP16	raw profiles	raw profiles with timestamp
	Camera: Sony Alpha 6000	video	video
Car 2 (Honda Pilot)	UWB: Pozyx (anchor)	-	ranges wrt moving agents
	GNSS: Topcon HyperVR, Novatel PwrPak7	positions	reference trajectory from GNSS and IMU integration and correction
	IMU: Epson G320 MEMS (built-in)	inertial information	
	LiDAR: Velodyne VLP16	raw profiles	raw profiles with timestamp
	Camera: GoPro HERO5	video	video
Car 3 (CyberCar)	UWB: Pozyx	ranges	ranges wrt static and moving agents
	GNSS: Topcon HyperVR, Novatel PwrPak7	positions	reference trajectory from GNSS and IMU integration and correction
	IMU: Epson G320 MEMS (built-in)	inertial information	
	LiDAR: Velodyne VLP16	raw profiles	raw profiles with timestamp
	Camera: GoPro HERO5	video	video
Pedestrian 1	GNSS: Topcon Hyper VR	positions	reference trajectory
Pedestrian 2	GNSS: Topcon Hyper VR	positions	reference trajectory
Cyclist 1	GNSS: Topcon Hyper VR	positions	reference trajectory
Cyclist 2	GNSS: Topcon Hyper VR	positions	reference trajectory

The *CONTEST* dataset aims at providing a common benchmark to research groups interested in this topic, and thus, supports testing and comparative performance evaluation of developed collaborative multi-sensor positioning approaches. The presented dataset is based on measurements acquired from platforms that were jointly moving in 2D and 3D space, which makes this benchmark unique and extremely useful. More specifically, the dataset contains data collected by both ground and aerial vehicles, acquiring reference (GNSS-based) trajectories, visual data, either as images or videos, LiDAR measurements and UWB ranges, mimicking both V2I and V2V communication.

2.3 Creating Reference Solutions

A key aspect of the data acquisition campaign was to obtain highly accurate GNSS-based platform trajectory data, which can be used as reference and also for various simulation scenarios. The ground platforms and drones primarily moved/flew predefined trajectories and rich sensor data was collected. The general pattern was to simulate traffic in a typical intersection area, where about 50% of traffic accidents happen. In these tests, there was no intention to use collaborative navigation software in real-time due to lack of reliable communication capabilities, and thus, everything was logged for post-processing. Figure 2 shows a test where, except from the UAS, all other platforms are visible.

Since the entire field campaign was conducted in open sky environment under good weather conditions in a low RF interference and multipath area, GPS/GNSS signal reception was excellent. Each of the four ground vehicles had two and the others one geodetic grade GNSS receiver each, while the drones had medium-grade multi-frequency receivers. Consequently, for the all the platforms highly accurate trajectories were computed. For two vehicles with high-quality IMUs, the platform attitude was also obtained. Unfortunately, for UAS 4 there was an unexpected hardware error, and only code-based accuracy was achieved. Table 2 Precision of post-processed GNSS/INS and GNSS solutions. list the precision of the trajectory estimation; note that the internally estimated precision is generally optimistic.

Table 2 Precision of post-processed GNSS/INS and GNSS solutions.

Platform	Solution Type	Position [m]		
		East	North	Height
GPSVan	GNSS/INS	0.001	0.001	0.003
Pilot	GNSS/INS	0.001	0.001	0.003
CRV	GNSS	0.007	0.006	0.013
CyberCar	GNSS	0.007	0.006	0.013
Cyclist 1	GNSS	0.007	0.006	0.012
Cyclist 2	GNSS	0.007	0.006	0.013
Pedestrian 1	GNSS	-	-	-
Pedestrian 2	GNSS	-	-	-
UAS1	GNSS	0.007	0.006	0.013
UAS2	GNSS	0.007	0.007	0.014
UAS3	GNSS	0.007	0.007	0.014
UAS4	-	-	-	-

The reference trajectories for the four drones and four vehicles are visualized in Figure 5. One drone, trajectory marked by yellow was in a fixed position to provide an overview image coverage of the entire area and thus allowing for visual tracking of all the other platforms, see Fig. 2.5a. The drone at mid-altitude, marked by blue flew a typical remote sensing data acquisition pattern. Finally, the two drones at the same lower altitude were flying close to each other to mimic delivery by drone situation. In Figure 5b, the trajectories of the four ground vehicles are added, showing the typical crossing and turning motion at intersection areas.

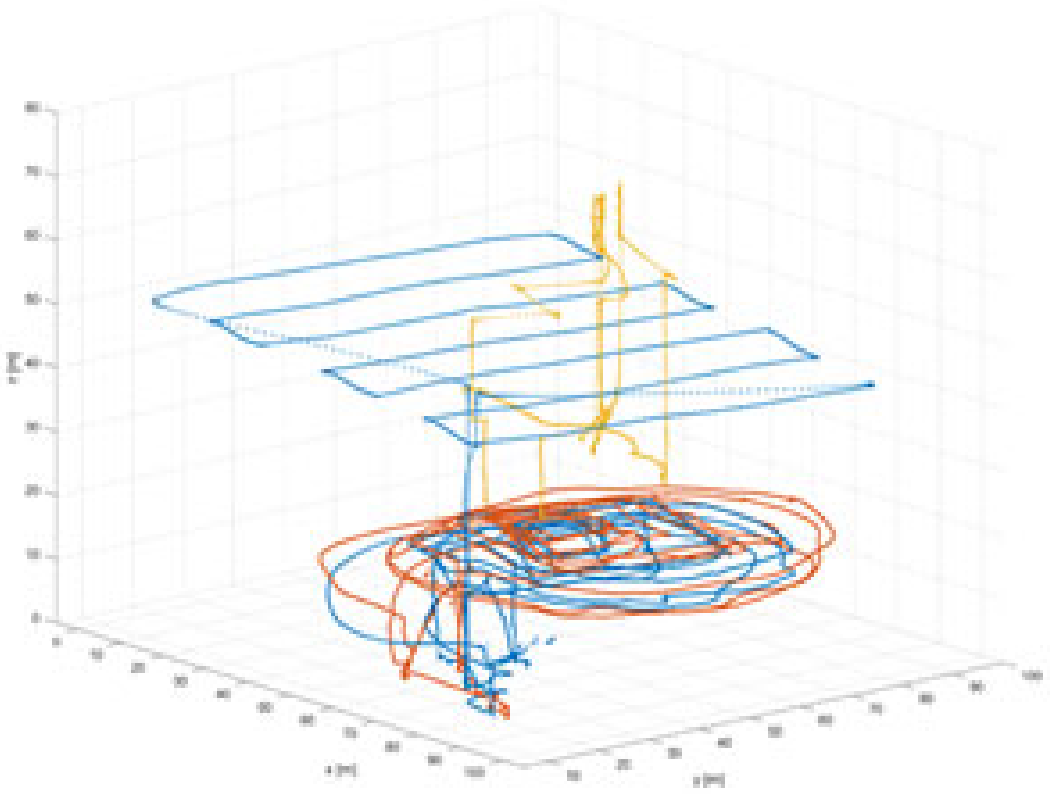

(a) Solutions for four drones

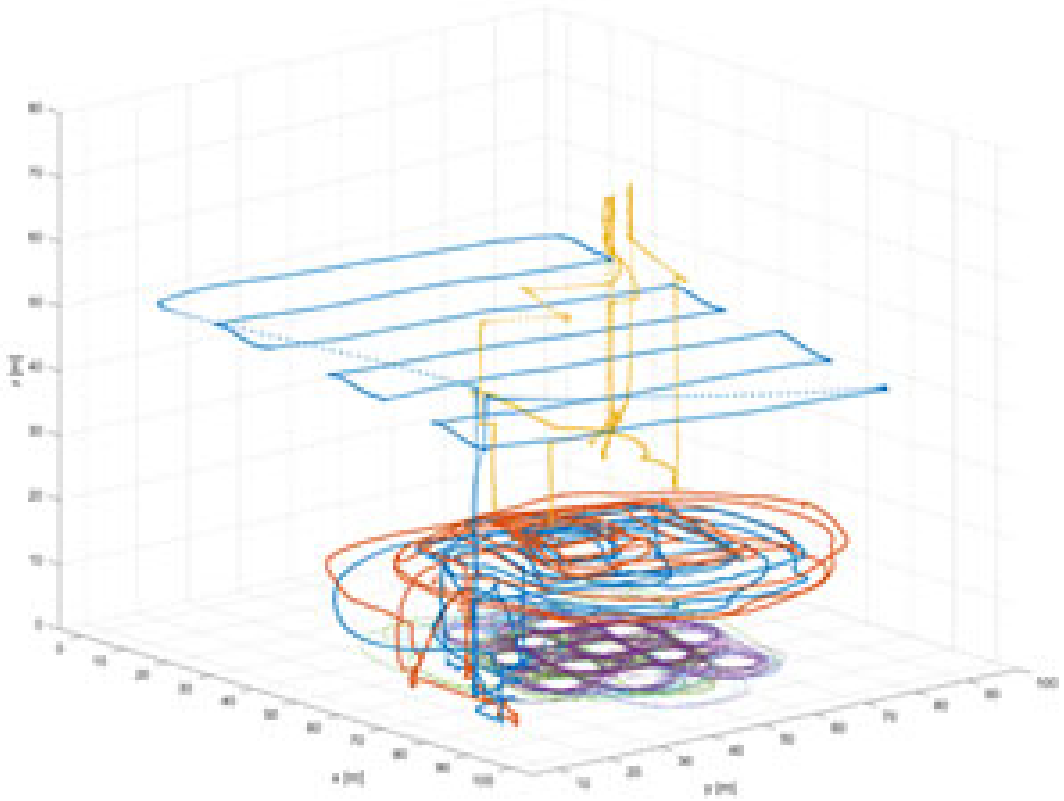

(b) Solutions for four drones and four vehicles

Figure 5 Reference GNSS solutions for four drones and four vehicles.

2.4 UWB Sensor Data Evaluation

UWB data was first used for creating collaborative navigation solutions, and thus, the quality of this dataset was thoroughly assessed. There are two key aspects of the UWB data streams: (1) the number of ranges observed, and then (2) the data rate of range measurements. Note that on the sensor level multiple measurements are performed to obtain a valid range, and thus, there is a ratio parameter to indicate the successful vs attempted measurements.

Figure 6 shows an example of ranges collected by four cars and four UASs over a 40-s time interval. From the figure it is quite clear that ground vehicles collected more ranges on average with the only exception of Car 2, which, differently from the others, acted as an UWB anchor, hence it was only involved in V2V ranging.

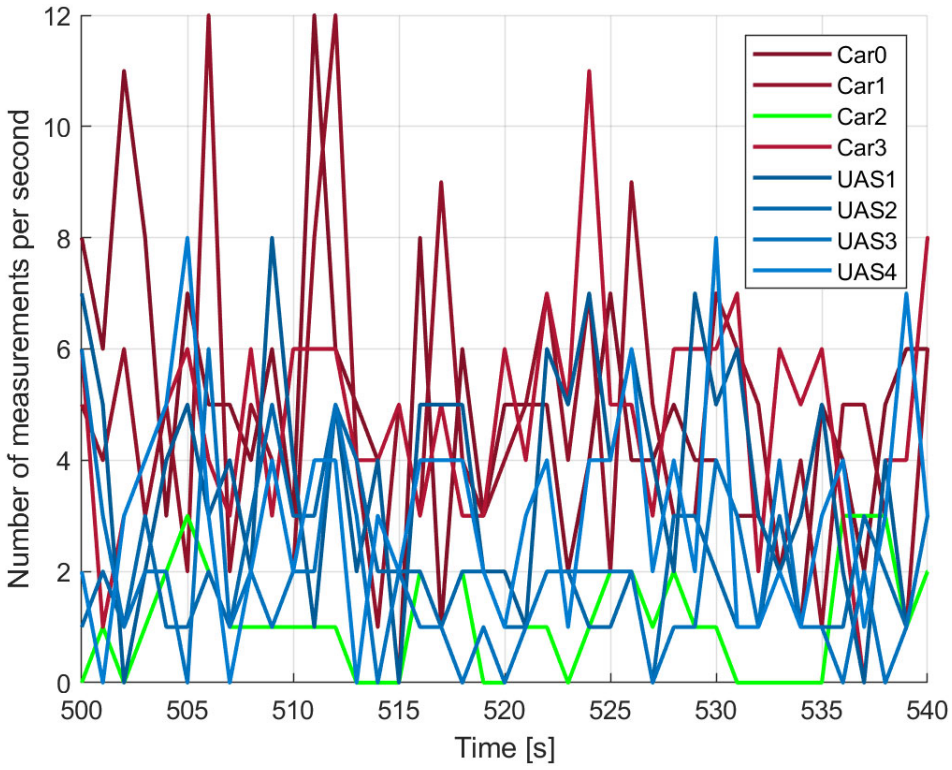

Figure 6 Range measurements of four cars and four UASs in a 40-s time interval.

Table 3 UWB ranging distribution (percentage with respect to the total number of UWB measurements). shows the distribution of the collected UWB ranges in terms of V2I and V2V measurements, distinguishing whether the measurements were collected from ground vehicles to infrastructure (G2I), aerial platforms vs infrastructure (A2I), or, in the V2V case, among the different combinations of ground (G) and aerial (A) platforms.

Table 3 UWB ranging distribution (percentage with respect to the total number of UWB measurements).

Range Category		Distribution of range measurements [%]
	G2I	42.7
V2I	**A2I**	19.5
	V2I total	**62.2**
	G2G	9.1
	A2A	9.5
V2V	**G2A**	6.8
	A2G	12.4
	V2V total	**37.8**

Table 4 UWB ranging data acquisition rate [range measurements per second]. reports the UWB statistics for what concerns the four cars and four UASs over a 1500-s time interval (the first part of the main test). A more comprehensive visualization of the number of

measurements per second is shown in Figure 7. Excluding Car 2, ground vehicles collected around 2.5 V2I ranges per second, whereas aerial platforms averaged only about one measurement per second. Interestingly, the average number of V2V ranges per second was approximately constant for all platforms (about 2).

Table 4 UWB ranging data acquisition rate [range measurements per second].

Platform	Mean	Std.dev.	Max
UAS1	2.4	1.9	12
UAS2	2.4	1.7	12
UAS3	3.4	2.5	14
UAS4	3.8	2.4	15
Car 0	4.7	2.5	15
Car 1	4.9	2.5	15
Car 2	1.4	1.2	8
Car 3	5.5	2.9	19

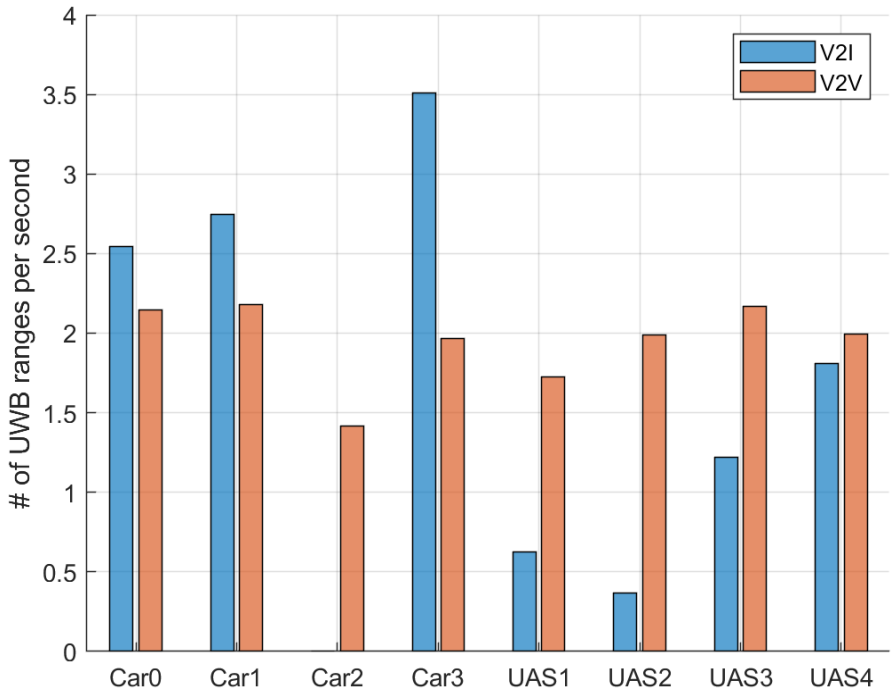

Figure 7 Comparison of V2I and V2V UWB measurements per second on the cars and UASs.

While the V2V ranges are quite evenly distributed, the inhomogeneous distribution of the V2I ranges, shown in Figure 7, needs more in-depth investigation. Figure 8 shows that certain anchors have a much lower contribution to the collected ranges, for example, the one on the top-left of the figure.

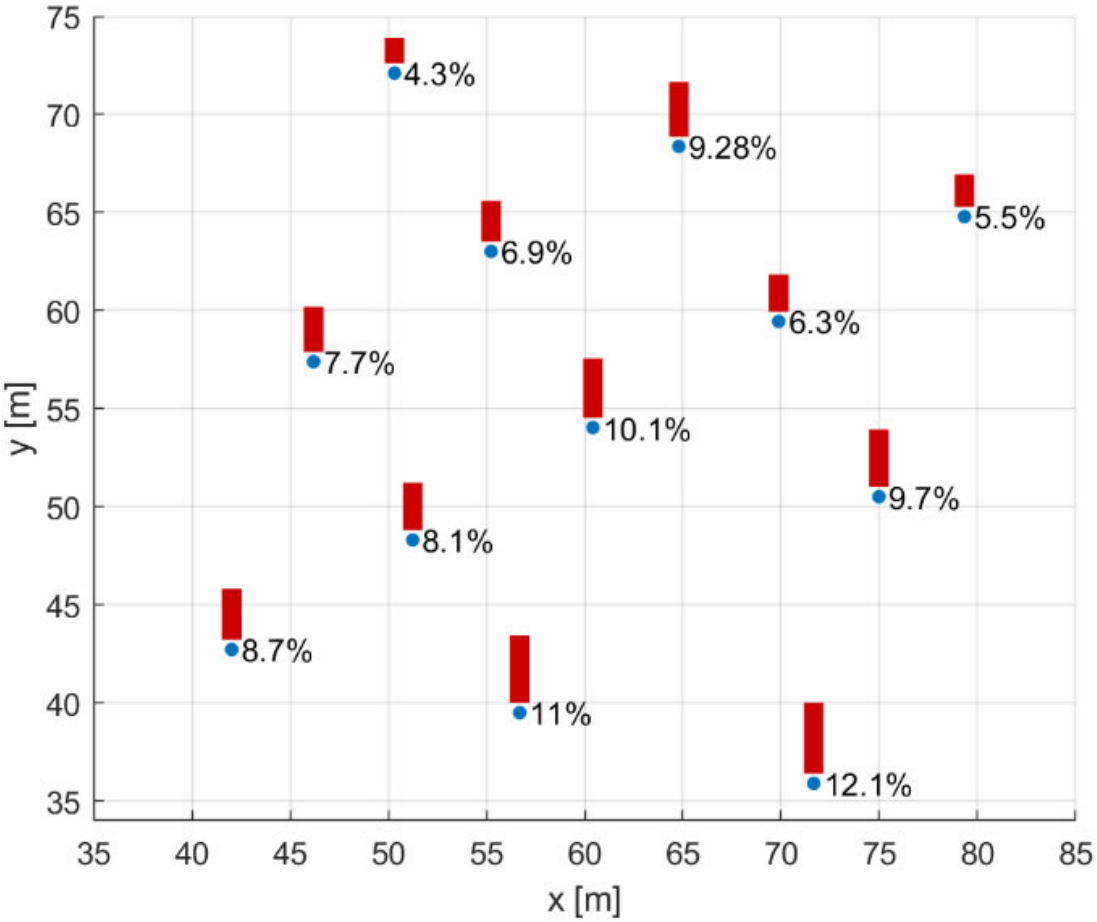

Figure 8 Distribution of the collected V2I ranges among the anchors.

However, according to the heat map of the ground vehicle locations, shown in Figure 9, this is probably simply due to the fewer vehicle trajectories close to such anchors. Furthermore, the lower amount of V2I ranges for the aerial platforms with respect to the ground ones shall be explained by the average distance of such platforms from the anchors. Indeed, as reported in Masiero et al. (2021), the UWB ranging success rate decreases with the distance between the involved devices. Moreover, comparing the ground and aerial platform heat maps in Figure 9 and Figure 10, it is quite clear that on average UASs flew at larger distances from the anchors than the ground vehicles. This is also confirmed by a comparison between UAS4 and the other UASs, as differently from the others, UAS4 flew at a higher altitude, at about 40 m from the ground vs 20 m for the others, but stayed at an almost constant horizontal location, approximately in the middle of the region covered by the anchors (white spot approximately in the center of Figure 10). This led to a higher V2I ranging success rate with respect to the other UASs, as shown in Figure 7.

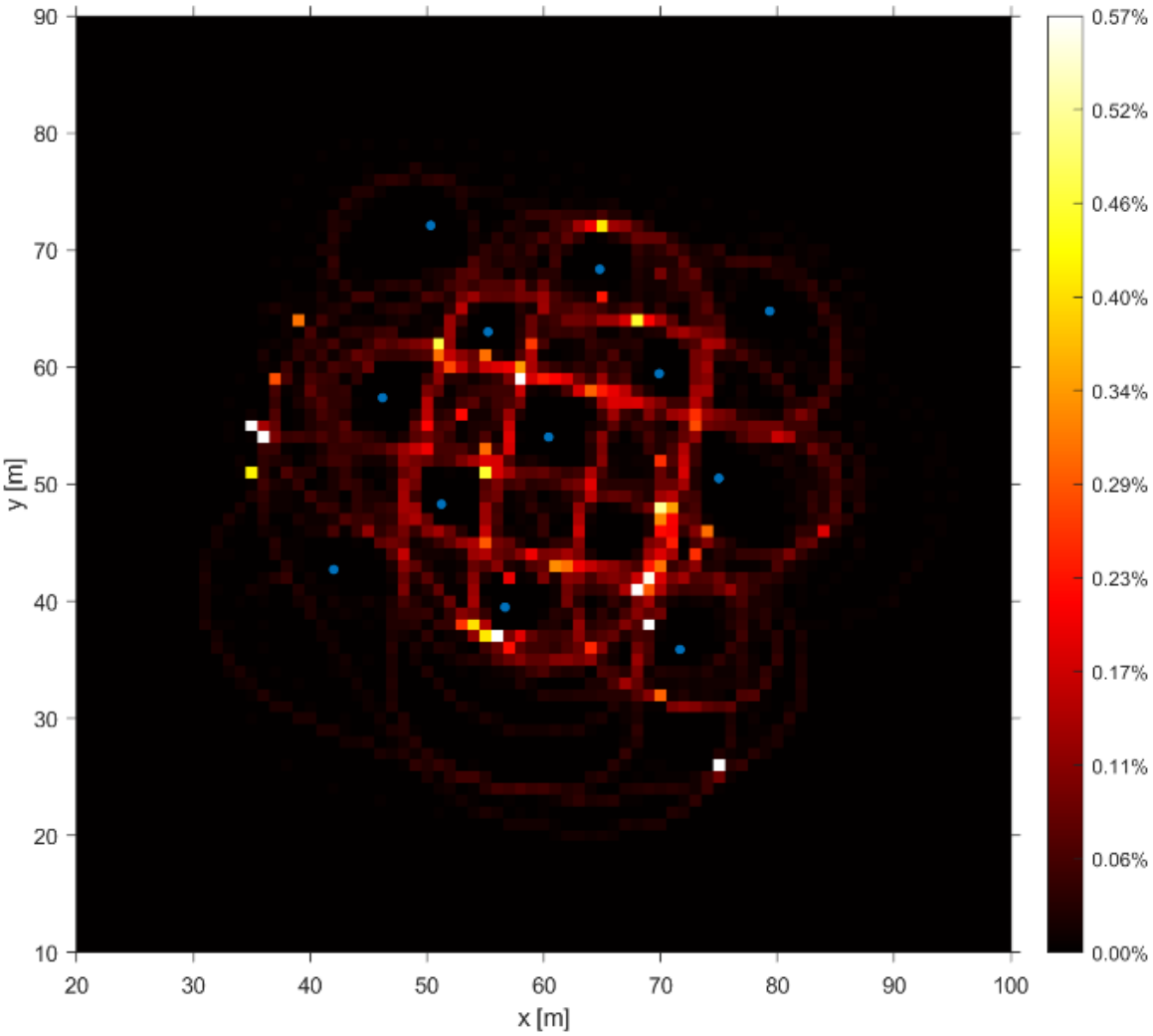

Figure 9 Heat map of ground vehicle tracks during the first part of the test; color visualization is saturated to the largest value in the color bar, and UWB anchors are represented as blue disks.

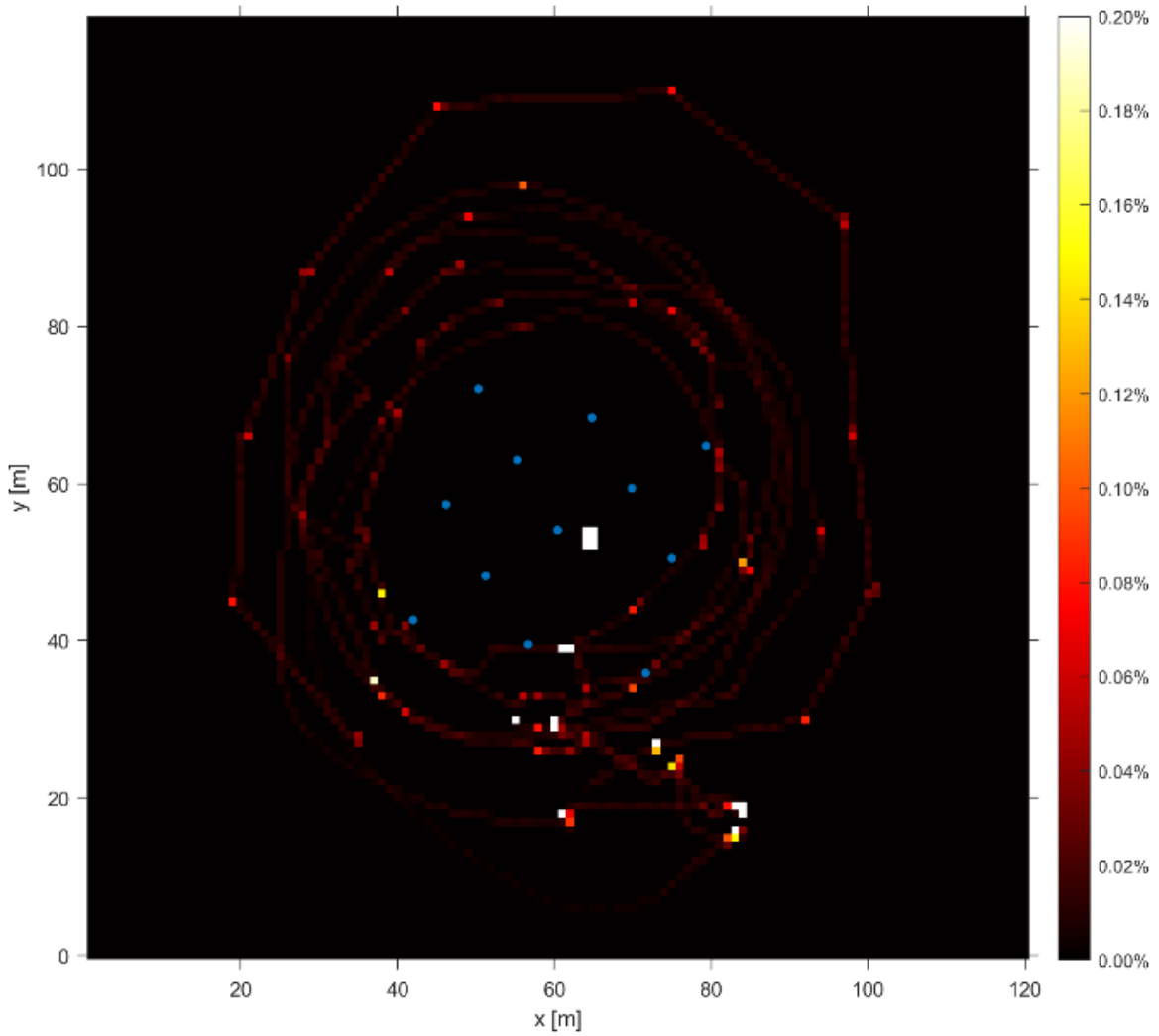

Figure 10 Heat map of UAS tracks during the first part of the test; color visualization is saturated to the largest value in the color bar, and UWB anchors are represented as blue disks.

2.5 Collaborative Navigation

The concept of collaborative navigation (CN) represents the next level of generalization of the sensor integration by integrating sensors deployed on multiple platforms (Lee et al., 2012; Buehrer et al., 2018). The two fundamental conditions of CN are the availability of inter-platform range and/or angular measurements and then communication to allow data sharing in real-time. There are several variations of the concept as well as their implementations. The key idea is that the platforms, aka nodes, form a geodetic network, and by using the inter-platform range/angular measurements, the relative positions can be estimated, i.e., the platform can be positioned in an arbitrary local coordinate system. The strength of the geometry of the network can be exploited in several ways, such as distributing accurate position information to nodes that have no or weak GNSS data, or detecting anomalies of individual node navigation solutions, such as jamming and spoofing, (Wang et al., 2022) or degraded range measurements, e.g., non-line-of-sight (Wang and Jiang, 2021).

A basic CN solution uses only inter-nodal range measurements either with or without other sensor data. In the former case, the ranges are used in the navigation filters, providing additional constraints. In the second case, the ranges are used to create a geodetic network (Ladai and Toth, 2022) and then the relative position information can be used as input to the individual or joint (federated) navigation filter. The main methods to solve this problem include:

- Static geodetic approaches, such as ordinary least squares (OLS), weighted least squares (WLS), etc. (Wang, 2023)
- Sequential estimators, such as conventional navigation filters (extended Kalman filters, particle filters, multiple mode filters, etc.), batch approaches (least squares “fitting” methods, solvers, SLAM, etc.).

In the first round, the UWB-based range measurements were considered as these data streams are available from almost all platforms; including ground vehicles, drones, and the static network. Since UWB technology uses extremely low power, the success rate of valid measurement fluctuates over a large range, depending on the environmental conditions. Figure 11 shows range measurements acquired for one and half hours by the UWB transceiver installed on the main vehicle, GPSVan and by half hours by UAS 4. The horizontal lines indicate when there was no motion, so ranges should not change. The areas with changing ranges represent three data collection sessions. In both static and moving state, there are outlier ranges, but the number of larger outliers is bigger when the sensor platform is in motion.

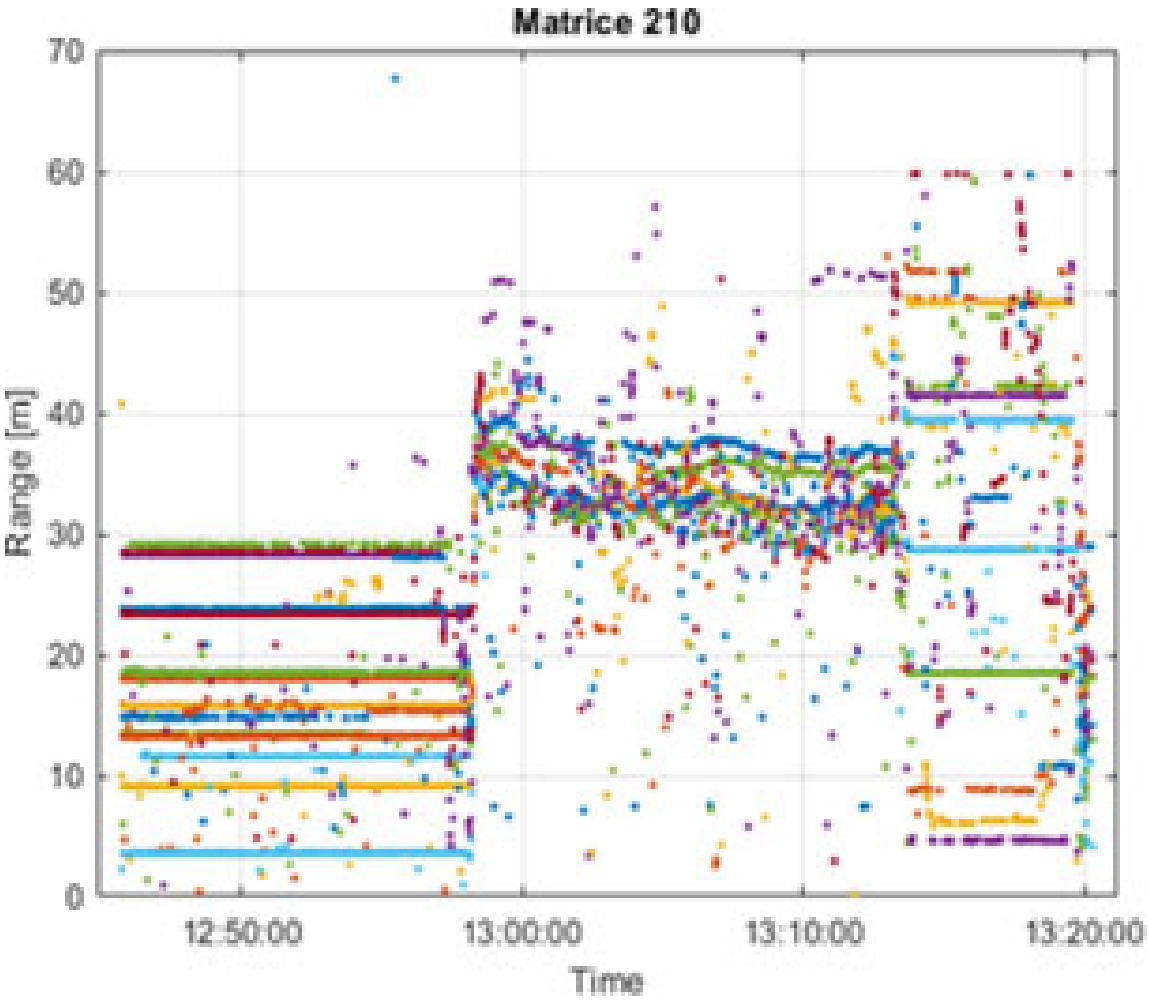

(a) Typical UWB range measurements from UAS4

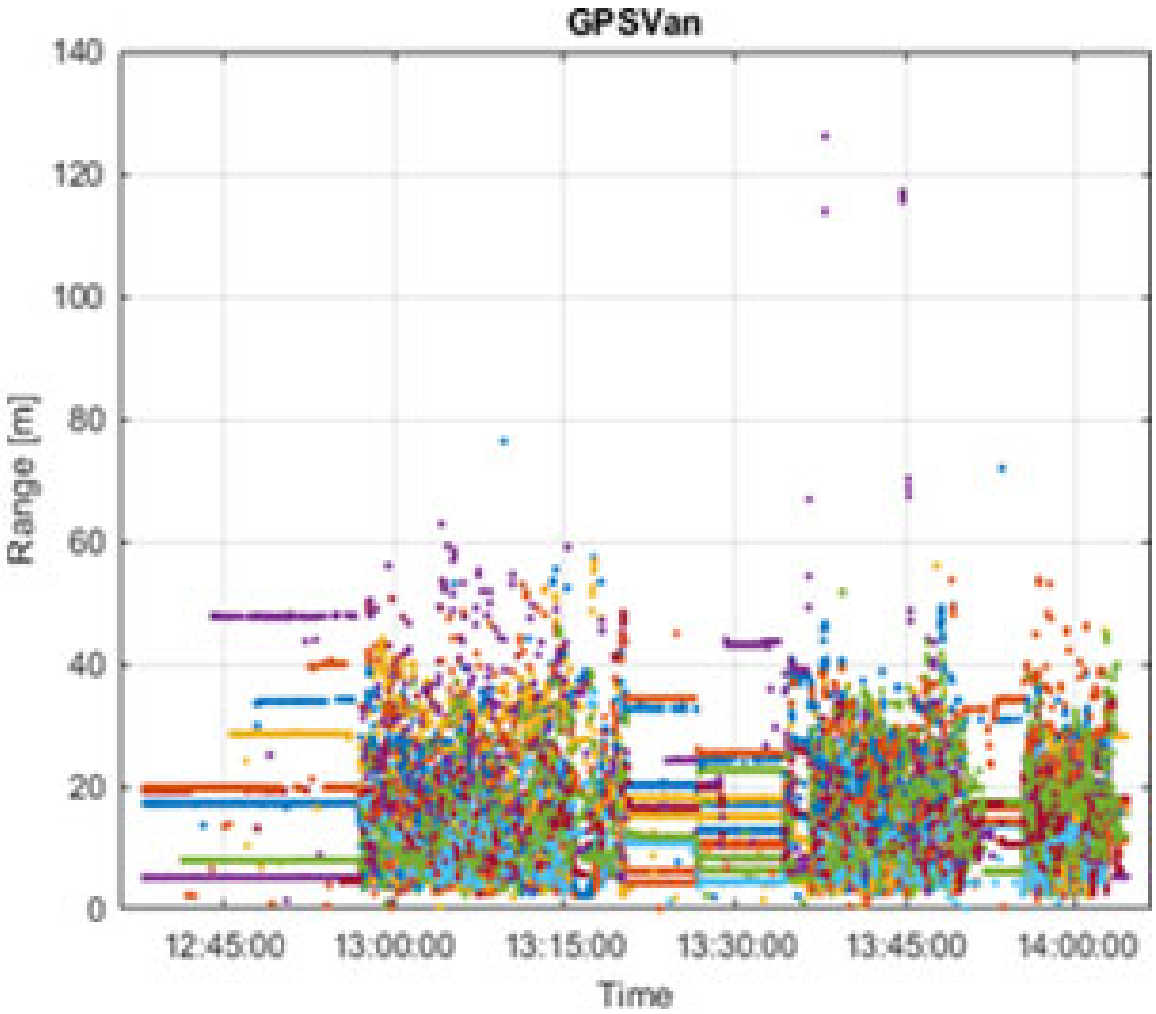

(b) Typical UWB range measurements from the GPSVan

Figure 11 Typical UWB range data acquired by two platforms.

A collaborative navigation-based solution for the four ground vehicles is similar to the reference solution in Figure 5b; at the scale of the figure, there is no visually noticeable difference. The three vehicles were positioned by using the infrastructure UWB system and the GPSVan was localized by both the ranging data from the three other vehicles and the infrastructure UWB transceivers. Figure 12 shows a few samples from the solution, where circles show that range measurements were available between the GPSVan and the infrastructure UWB transceivers. Figure 12a shows the GPSVan outside of the UWB network, and while there are six circles, they intersect at small angles, so the positioning accuracy is not good. Note that another vehicle is also outside. Figure 12b depicts the case when the GPSVan is along the boundary of UWB network. There are only three circles, and the three vehicles are inside, yet they are almost along a line, so the accuracy is still not good. Figure 12c shows a good case when all vehicles are inside of the UWB network and there are six circles with several near perpendicular intersections, resulting in an accurate position. Figure 12d represents a case which is similar to Figure 12b, except there are four circles with better intersections, resulting in good accuracy. In general, the positioning accuracy is in the few-decimeter range, which means the detection of PNT anomalies larger than one meter can be reliably detected.

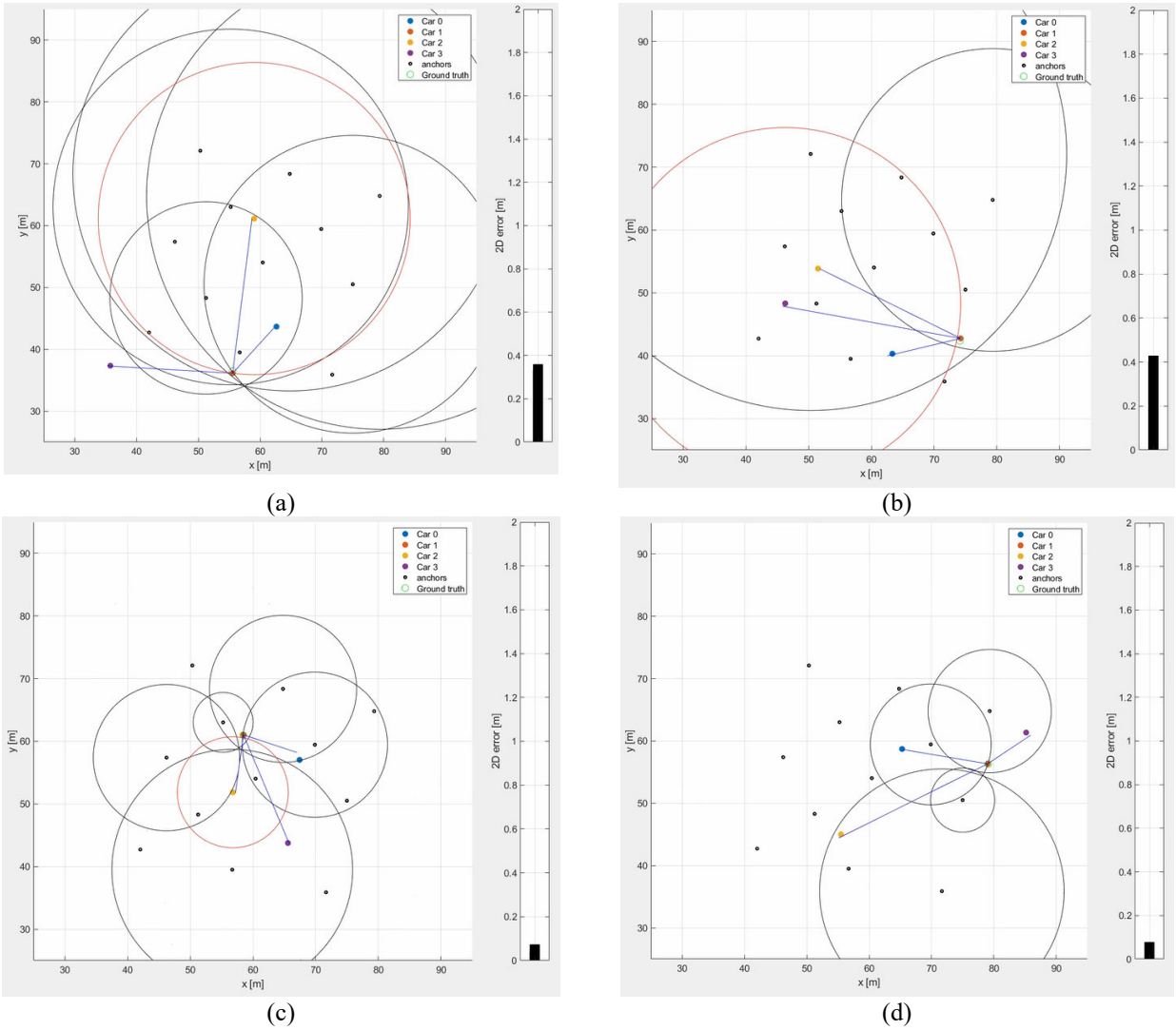

Figure 12 Collaborative solution at four epochs.

The vertical bars on the right in Figure 12 show the internally estimated positioning precision; Figs. a-b depict poor performance, while c-d demonstrate good performance under favorable conditions. Figure 13 shows the estimated positioning precision of an about 1-minute run; the horizontal axis is in epochs and the vertical is in m. This decimeter-level positioning performance is clearly adequate for transportation applications; even for lane-following it is suitable.

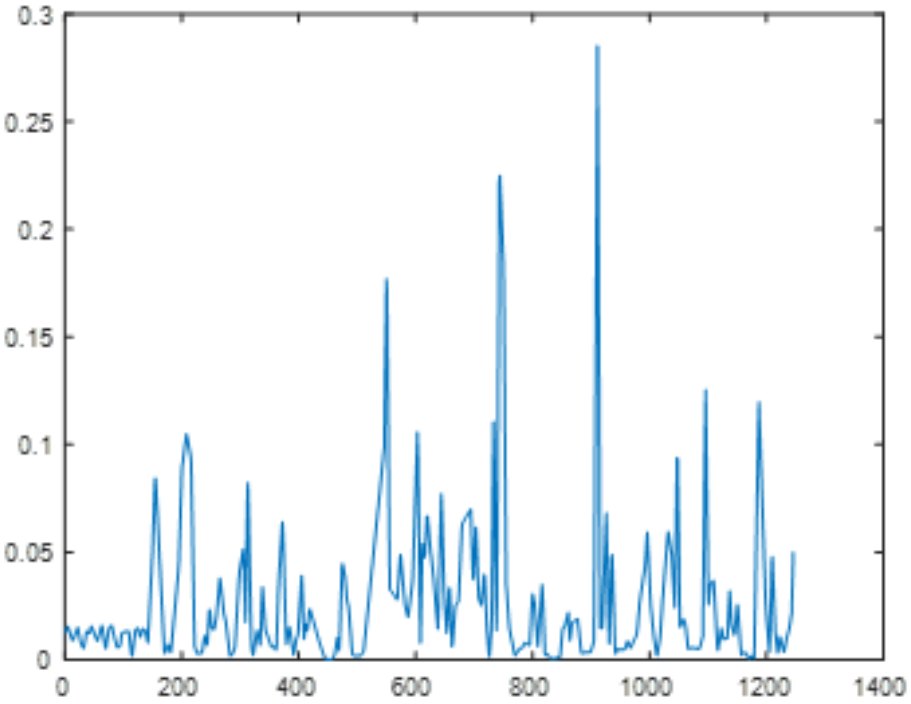

Figure 13 Internally estimated positioning precision in 2D.

3 Highly Automated Vehicle Threat Testing

3.1 Introduction

Terrestrial radionavigation systems (TRNS) provided the primary navigation infrastructure before GPS was introduced, and then they have seen a decline as GPS became of the primary workhorse of navigation worldwide. Given the increasing vulnerability of GPS/GNSS, there is a renewed interest in TRNS, using state-of-the-art technologies. In cooperation with NextNav, using their Metropolitan Beacon System (MBS), dataset was acquired to support performance testing and assessing resilience capabilities against possible threat scenarios in urban environment.

Central to the transportation revolution that will be driven by urban air mobility (UAM) is the problem of robust and secure navigation. Urban environments offer more challenges, such as interference and multipath, when compared to open sky conditions. As the only positioning system that offers absolutely referenced meter-level accuracy with global coverage, GNSS will no doubt play a significant role in this revolution. If strengthened against jamming and spoofing, carrier-phase differential GNSS (CDGNSS), coupled with low-cost inertial sensing, will be nearly sufficient for position, velocity, and timing (PVT) needs. But nearly sufficient is insufficient: it is not enough for a UAM PVT solution to offer decimeter-accurate positioning with 99% availability, or even 99.9% availability. UAM will demand that its navigation systems offer dm-accurate positioning with integrity risk on the order of 10^{-7} for a meter-level alert limit and availability with several more 9s than 99.9% (Tenny and Humphreys, 2022). This effort introduced a method of tightly coupling carrier-phase-differential GNSS (CDGNSS) with TRNS signals and data to build a robust positioning, velocity, and timing (PVT) solution for UAM, which requires precise and robust PVT solutions that are resilient to interference and jamming. Reference data was acquired in cooperation with NextNav. This activity was originally reported in [7].

3.2 Data Acquisition

The test data was acquired in Bay Area, where NextNav operates a network of TRNS transmitters, see Figure 14. The aerial test vehicle from UT Radionavigation Laboratory was a DJI Matrice 300 multi-rotor vehicle with a variety of sensors mounted on the vehicle, including a dual antenna GNSS L1 receiver, a NextNav TRNS receiver, and a Bosch BMX055 consumer grade IMU, see Figure 15. In addition, a GNSS reference receiver was placed near the planned flight location. The acquired dataset contains dual antenna GNSS L1 double differenced pseudoranges, carrier phase measurements, TRNS position solution, TRNS pseudoranges, calibrated barometric pressure sensor measurements, and inertial sensor measurements. The reference and aerial test vehicle GNSS receivers utilized the RNL's RadioLynx, GNSS front end with a 5 MHz bandwidth, and was processed with the PpRx software-defined GNSS receiver (SDR).

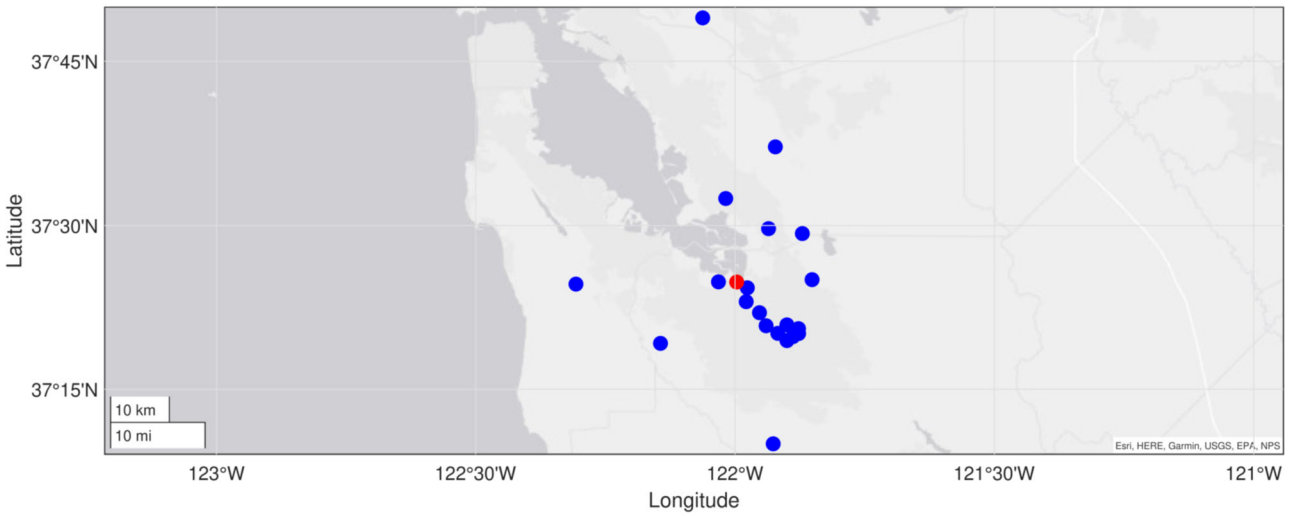

Figure 14 Map of the location of the TRNS transmitters visible to the TRNS receiver during flight and the flight location in red.

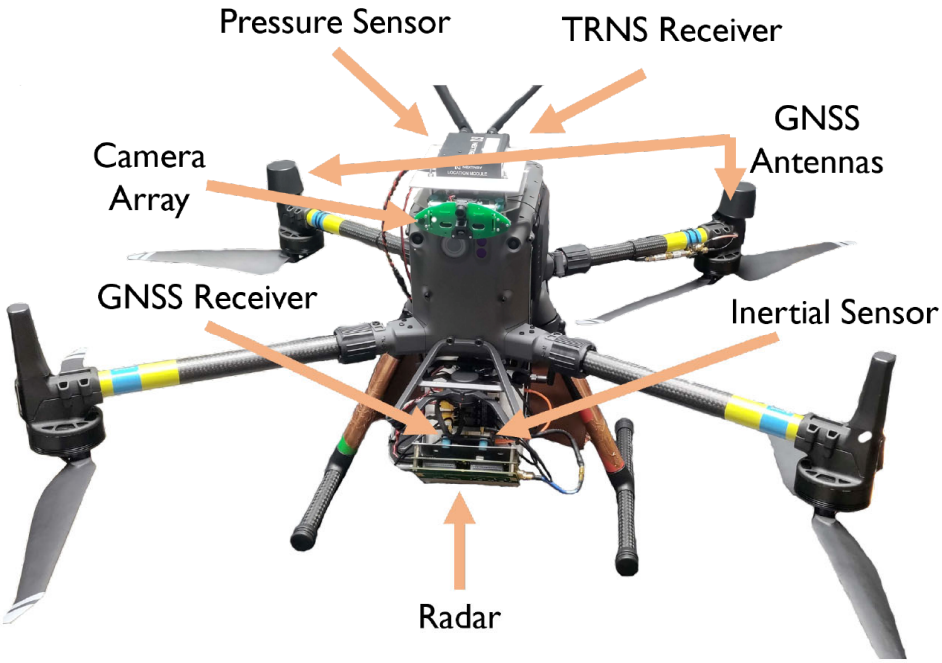

Figure 15 UT RNL's aerial test vehicle, carrying two single frequency GNSS antennas, a radar sensor, TRNS receiver, pressure sensor, and three cameras.

A data collection flight was performed in an area where NextNav TRNS signals are available (Figure 16). The flight path was limited to 80 meters by 100 meters in the east and north directions due to constraints on communication range with the UAS. Note that FAA regulations limited the altitude ceiling to 121 meters above ground level. The full flight path shown in Figure 16. The recorded dataset includes approximately 900 seconds of data at different altitudes and varying vehicle velocities.

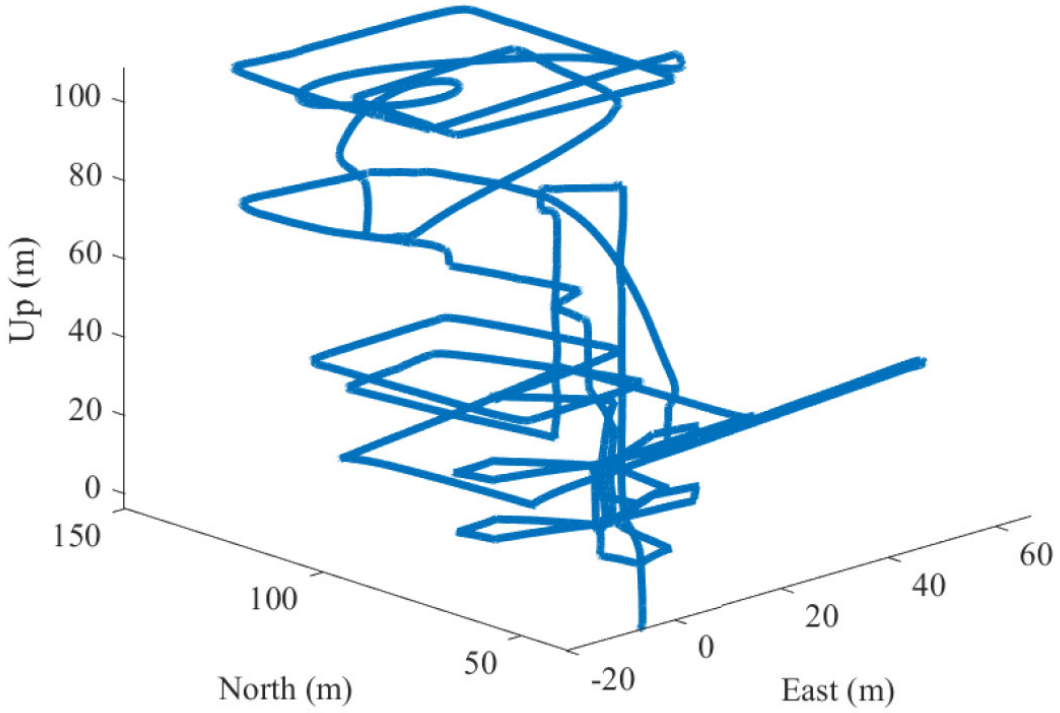

Figure 16 Flight path of the aerial vehicle during data collection flight. The position is shown in meters from the phase center of the reference receiver antenna in the ENU frame.

3.3 Results of analyzing TRNS pseudoranges

The TRNS pseudoranges were analyzed using the collected dataset and the tightly-coupled version of PpEngine. The estimated TRNS transmitter clock offsets (Figure 17) were observed to determine the behavior of the TRNS transmitter clocks. The estimated transmitter clock offsets were found to be non-zero and unique to each transmitter. The largest difference between transmitter clock offsets indicates that the transmitter clocks differ by as much as 30 nanoseconds. These estimated TRNS transmitter clock offsets are not fully observable meaning part of the estimate may be due to the TRNS receiver clock offset. The TRNS pseudorange innovations (Figure 18) were examined and found to be nearly zero-mean and white, demonstrating that the pseudorange errors were well modeled. This shows that despite the lack of full observability of the clock offsets, the location of the TRNS receiver can still be estimated.

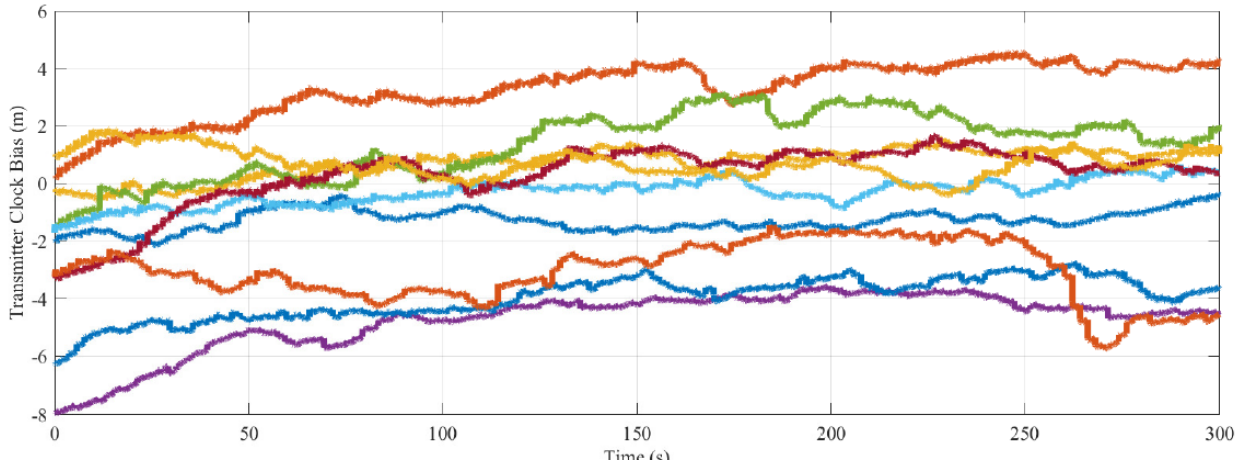

Figure 17 Estimated TRNS transmitter clock offset of the TRNS transmitters in meters.

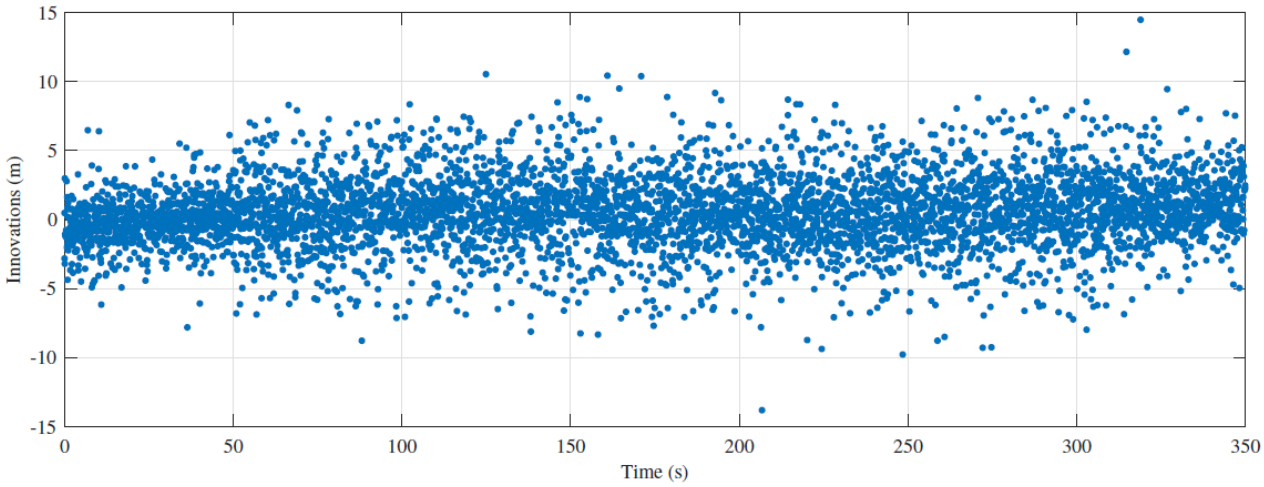

Figure 18 TRNS pseudorange innovations in meters.

3.4 Artificial GNSS Outage

A long scale GNSS outage experiment was preformed to represent a worst-case scenario of a full loss of GNSS availability. The experiment was performed for both loosely- and tightly-coupled estimators. The loosely-coupled solution (Figure 19) shows that during a long duration GNSS outage a bias between the CDGNSS position and TRNS position arises. During this outage the estimated error standard deviation was 1 meter in both the east and north directions. The experiment was repeated utilizing the tightly-coupled estimator (Figure 19). During the outage the estimated error standard deviation was 2 meters in both the east and north directions. The tightly-coupled estimator has a similar offset from the CDGNSS position solution showing that there is an unknown source of error in the TRNS network causing the offset of the TRNS position solution.

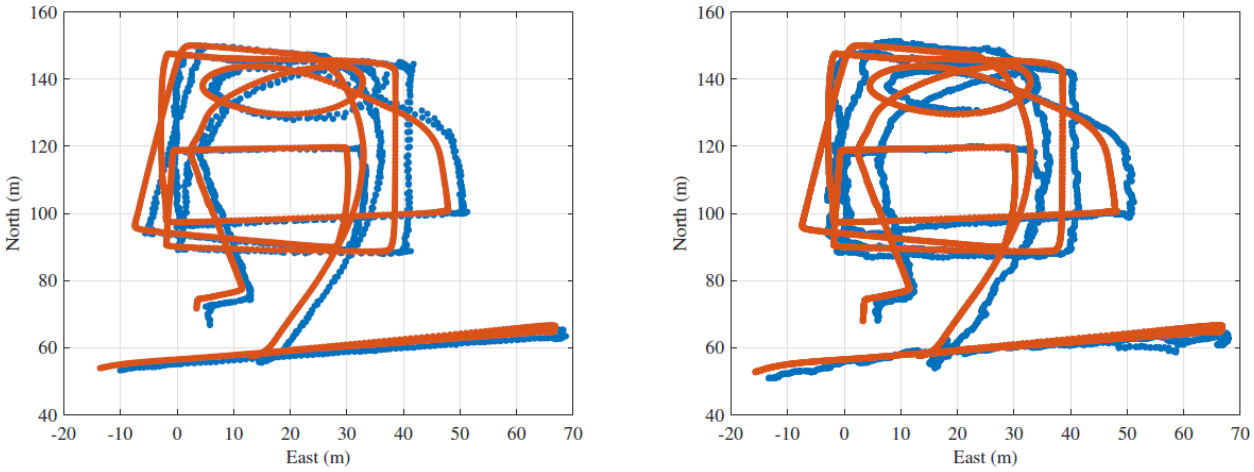

Figure 19 Left: The blue is the loosely-coupled TRNS position solution during period of artificial GNSS outage. The orange is the CDGNSS position. Right: The blue is the tightly-coupled TRNS position solution during period of artificial GNSS outage. The orange is the CDGNSS position.

3.5 Intermittent Artificial GNSS Outages

A UAM vehicle will likely only face interference or a loss of GNSS availability for a portion of the flight. A test of intermittent GNSS availability was performed by artificially suppressing GNSS measurements from entering the estimator for a duration of 30 seconds with a 60 second period. The estimator was first tested with a series of intermittent GNSS outages without the addition of the TRNS measurements (Figure 20). The error grows in the position during the outage is exponential. The exponential error growth is cause by drift in the consumer grade inertial sensor. During the short duration outage, the 1-σ uncertainty grew to 28 meters in the east and north directions, and 8.4 meters in the Up direction. The maximum error during the test was found to be 166.7 meters, demonstrating the need for the addition of TRNS to constrain the error growth during GNSS outages.

A UAS will likely only face interference or a loss of GNSS availability for a portion of the flight. A test of intermittent GNSS availability was performed by artificially suppressing GNSS measurements from entering the estimator for a duration of 30 seconds with a 60 second period. The estimator was first tested with a series of intermittent GNSS outages without the addition of the TRNS measurements (Figure 20).

The error grows in the position during the outage is exponential. The exponential error growth is caused by drift in the consumer grade inertial sensor. During the short duration outage, the 1-σ uncertainty grew to 28 meters in the east and north directions, and 8.4 meters in the up direction. The maximum error during the test was found to be 166.7 meters, demonstrating the need for the addition of TRNS to constrain the error growth during GNSS outages.

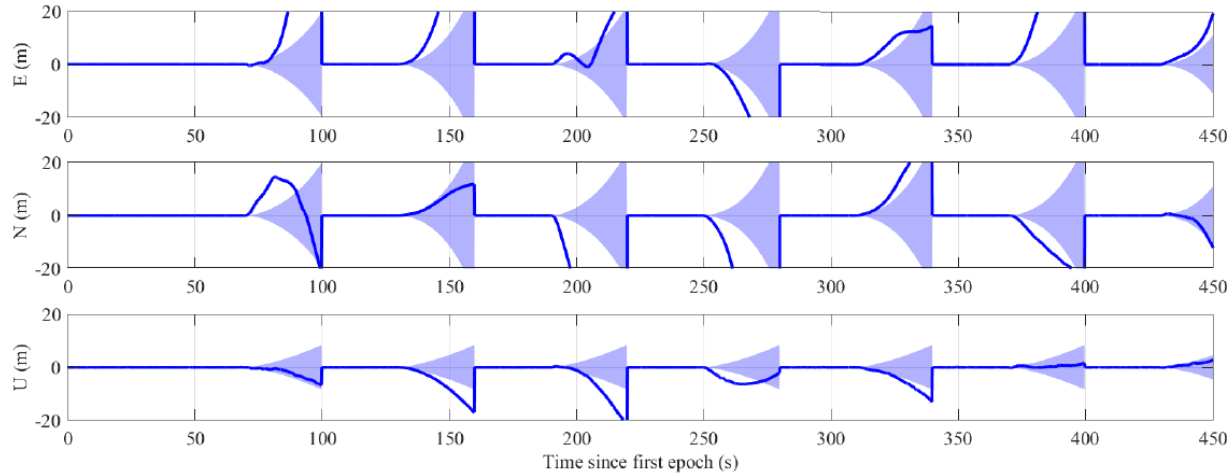

Figure 20 Intermittent periods of artificial GNSS and TRNS outage. The solid blue shows the position errors in meters in the ENU frame due to the inertial sensor. The shaded region is the 1-σ uncertainty.

The intermittent GNSS outages test was then preformed with the addition of TRNS measurements. The same interval was used so the tightly-coupled and loosely-coupled estimators could be directly compared to one another. For both tightly- and loosely-coupled estimators the addition of TRNS measurements served to constrain the error growth during GNSS outages (Figure 21).

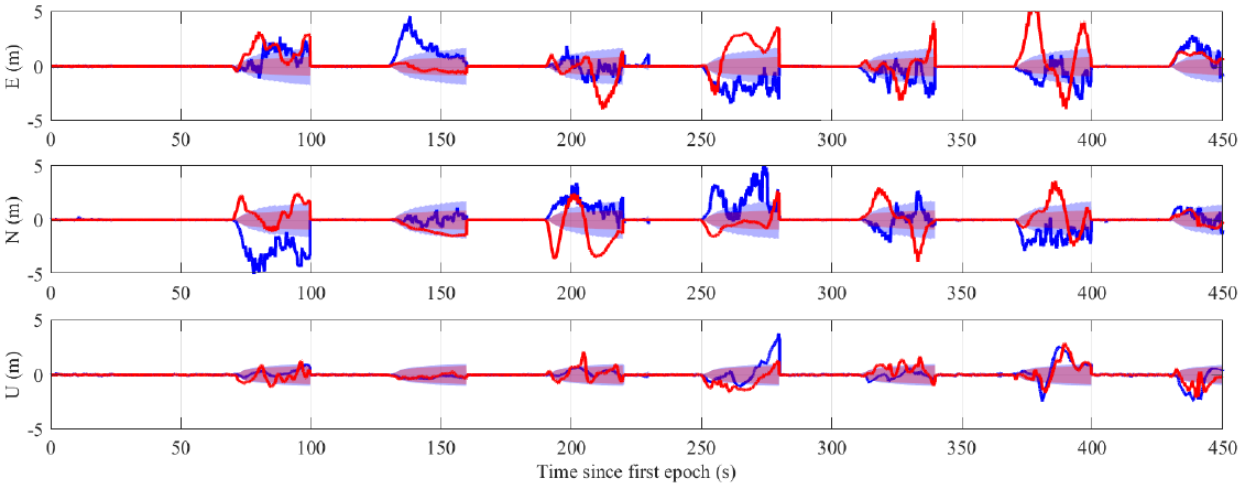

Figure 21 Position errors in meters in the ENU frame during intermittent periods of artificial GNSS outages. The solid line is the error of the position estimate, and the shaded region is the 1-σ uncertainty. The blue shows the tightly-coupled estimator while the red shows the loosely-coupled estimator.

The loosely-coupled estimator 1-σ error uncertainty grew to 1 meter in each direction. In contrast, the tightly-coupled estimator 1-σ error uncertainty grew to 1.5 meter in the east and north directions while only growing to 1 meter in the Up direction. The tightly-coupled estimator had a larger uncertainty due to the unknown TRNS transmitter clock offsets. Both

estimators had very similar behavior in the Up direction due to the poor vertical dilution of precision causing the position estimate in the Up direction to be heavily weighted by the pressure measurements.

In summary, TRNS provides a backup PNT source that can be utilized during GNSS outages to constrain the error growth of an inertial sensor. This study demonstrates the first use of tightly-coupled CDGNSS, TRNS, and inertial sensing to provide a robust PVT solution on an aerial vehicle. An innovations-based measurement exclusion technique mitigates the impact of TRNS multipath errors and pressure anomalies. Based on a comparative analysis of loose- and tight-coupling on a UAS during simulated GNSS outages, it was found that during short duration GNSS outages the 1-σ position error in the east and north directions were 1 meter and 1.5 meters for the loosely- and tightly-coupled estimators, respectively. This performance is adequate for several transportation applications but for decimeter-level positioning or detecting disturbances and threat to a PNT system, additional sensor data and geospatial information are needed.

4 PNT Integrity Monitoring

4.1 Introduction

We will study modern receiver autonomous integrity monitoring (RAIM) techniques which should harness significant benefits from the GPS III extended data structure as well as from using multiple GNSS constellations. Since certain data messages are not yet declared operational and constellations are incomplete, these efforts will be primarily based on simulations. In addition, we will extend RAIM to incorporate terrestrial and LEO satellite SOPs when available. Scenarios in various combinations, including multipath, signal blockage, and jamming and spoofing will be evaluated. Since the team has a full spectrum of GPS/GNSS receivers, actual tests will be conducted to assess the developed methodologies and practices for standardized testing. These tests, including laboratory and in situ sessions, will be primarily land vehicle based. The outcome of these investigations will be in a sense complementary to the DHS Best Practices document, which is focused on static receiver deployment and protection with guidelines for users and manufacturers. This activity was originally reported in [8-11].

4.2 Integrity

Integrity was introduced in aviation field to evaluate the performance of GNSS with the help of Airborne Based Augmentation System (ABAS), Ground Based Augmentation System (GBAS), and Satellite Based Augmentation System (SBAS). When GNSS range measurements are exclusively used, ABAS is usually referred as Receiver Autonomous Integrity Monitoring (RAIM) (Zhu et al., 2018). With the advancement of autonomous driving, the integrity monitoring of GNSS navigation for ground vehicles has become more and more important, especially for the safety- and liability-critical applications. Advanced Receiver Autonomous Integrity Monitoring (ARAIM) is being developed in recent years to incorporate multiple frequencies and satellite constellations across all major GNSS constellations (Blanch et al., 2013, 2017, 2019b).

Table 5 Basic characteristics of RAIM and ARAIM.

	RAIM	**ARAIM**
Signals	GPS L1 CA only	GPS L1-L5 + Galileo E1-E5a (at least)
Integrity parameters	Fixed	Broadcast in Integrity Support Message (ISM)
Fault probabilities	Fixed	Variable
Integrity assessment	Fixed probability of missed detection (10^{-3})	Variable probability of missed detection
Effect of temporal decorrelation	Only discussed for false alert rate	Taken into account explicitly (integrity and continuity)
Exclusion function effect on integrity	Probability of missed detection is not modified to account for the exclusion function	Integrity risk explicitly includes the effect of exclusion

The receiver level integrity monitoring is mostly solved as a hypothesis testing problem (Lee, 1986; Brown and Chin, 1997; Joerger *et al*., 2014; Yang and Xu, 2016; Maaref et al., 2018; Zhu *et al.,* 2020; El-Mowafy *et al*., 2020), though there are recent efforts to employ machine learning in the developed algorithm (Temple, 2006), aiming to be able to meet the integrity requirements of Category I, II, and III precision approach using combined GPS and Galileo constellation. In the conventional hypothesis testing technique (Joerger *et al*., 2014), the least-squares-residual-based (RB) and solution separation (SS) are the two widely used RAIM methods in safety-critical applications. RB RAIM uses a single test statistic for fault detection in the measurement domain, whereas the SS RAIM adopts multiple test statistics tailored to the fault hypothesis and to the state of interest in the position domain. The superiority of SS RAIM, however, is outweighed by conservative assumptions for computation efficiency and ultimately RB RAIM provides tighter bounds on integrity risk. The two typical implementations are the snapshot approach that is usually based on the residuals of least squares (LS) estimator for observations of the current epoch, and the other is the sequential approach, which is usually based on innovation of Kalman filter (KF) that uses both current and past observations (Zhu et al., 2020).

4.3 Detection/Mitigation Approaches

Looking at the integrity monitoring problem from a PNT system level perspective, there are several options for detecting and mitigating anomalies, either unintentional or intentional ones. A somewhat high-level classification is provided below:

1. GPS/GNSS system level
   - Signal structure (authentication)
   - Signal power and diversity in GNSS
2. GPS/GNSS receiver level
   - Antenna design
   - Receiver integrity monitoring (RAIM/ARAIM)

- Various integrity parameters and events

3. PNT system level
   - IMU integration
   - Environment-based approaches
   - Sensor integration (onboard)
   - SooS technologies (RF)
   - Using geospatial data (maps, for example, Google's Live View)
   - Collaborative navigation/cooperative sensing (in inverse)

The integrity monitoring support provided on the system level (1) is beyond user control, and it is part of the continuous modernization effort of GNSS. The receiver level integrity monitoring (2) has been addressed elsewhere. Here the focus primarily is on the PNT system level (3), which has many options. The classical navigation sensor integration is based on fusing GPS/IMU data and, more recently, additional sensors are included, such as imaging, RF and SooS technologies. Some of these topics are discussed in other sections of this report. Here we consider the exploitation of the collaborative navigation concept, which represents the next level of generalization of the sensor integration by integrating sensors deployed on multiple platforms. In most applications, in particular normal vehicle traffic on the road network, it is very rare that platforms navigate alone. In fact, the opposite is truer that the roads are overloaded and, many times, congested. Therefore, collaboration of vehicles is necessary to improve safety and increase traffic flow.

The collaborative navigation concept introduced earlier was founded on the idea to share navigation information for a group of platforms sharing close proximity with the objective to achieve better navigation for the all the platforms. However, it can be used in the other direction, namely checking individual platform navigation solutions against a joint navigation solution based on a group of platforms, and thus detecting any anomalies and, potentially, offering mitigation.

4.4 Exploiting of collaborative navigation

There are multiple ways how the geometric strength of a geodetic network formed by platforms can be exploited for detecting PNT solution anomalies caused by RF interference, such as lack of GNSS signals, jamming and spoofing. The concept for a simple example is shown in Figure 22, where four platforms form a network and one of the vehicles PNT solution is compromised. The upper row shows that using range data in combination with individual platform PNT solution, the spoofed solution will be pulled closer to the correct solution at the price of errors introduced at three other solutions; this is what the adjustment does, i.e., distributing the differences evenly. Using outlier detection techniques, the spoofed node can be detected, provided the shift is large enough. In contrast, using a range only solution, the network preserves the correct relative positions, but it is floating, i.e., the orientation is unknown with respect to the navigation frame. Using graph matching, the spoofed node can be easily detected, and

based on that the correct position can be computed using the three correct individual PNT solution in combination with the range data.

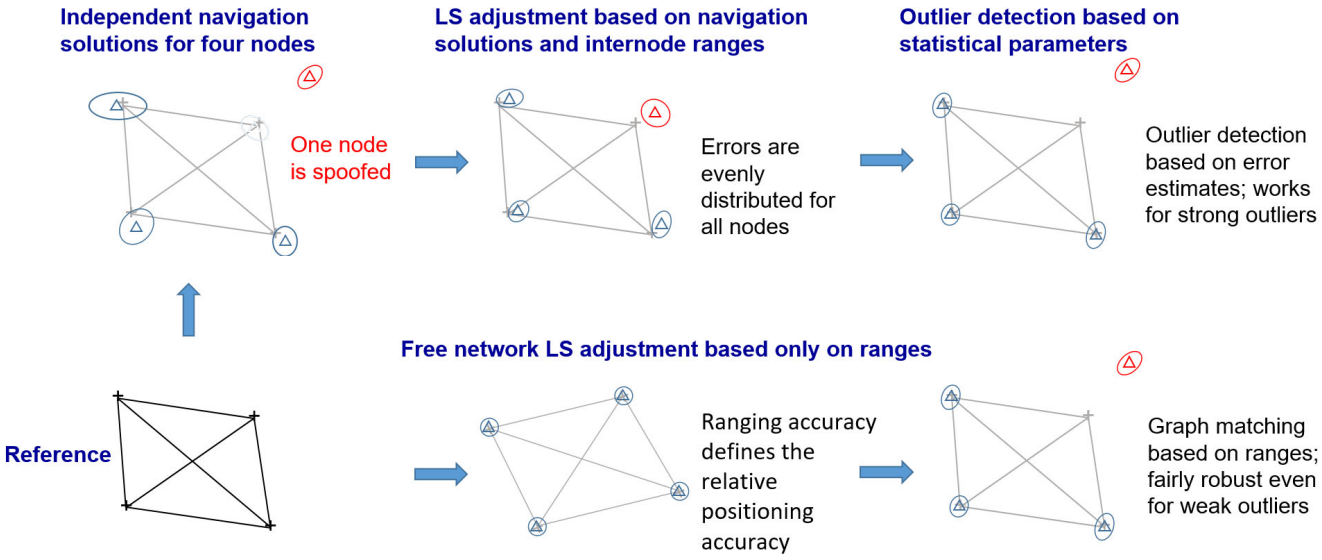

Figure 22 Four-platform collaborative navigation with one node spoofed.

There are several ways to create collaborative navigation solutions, which are listed below:

1. Snapshot/static geodetic approaches:
    - Ordinary least squares (OLS),
    - Weighted least squares (WLS), etc.
2. Sequential estimators:
    - Navigation filters:
        - Kalman Filters (KF),
        - Extended Kalman filters (EKF),
        - Particle Filters (PF)
        - Multiple Mode Filters, etc.
    - Batch approaches:
        - Least squares “fitting” methods
        - Solvers, e.g., non-linear least squares
        - SLAM

Group (1) represents a totally independent solution for the relative position of the nodes at an epoch (Wang et al., 2022). In contrast, Group 2 uses information from past epochs, such as the previous epoch for the classical navigation filters or more previous epochs for the batch approaches. Note that Group 2 solutions are based on using the local PNT solutions with the range measurements.

4.5 Single outlier detection

To assess the performance of the collaborative navigation approach for single outlier detection, the centralized integration architecture was adopted by assuming the GNSS solution of four vehicles as well as the V2V and V2I range measurements are available to a central EKF without any communication delay. GNSS solutions of four vehicles, V2I ranges from vehicle A, and V2V ranges among four vehicles are the measurements for the EKF. The state vector includes two dimensional positions, velocities, and accelerations of these four vehicles. Figure 23 shows the trajectory of a test run by vehicle A (GPSVan) and the V2I anchor nodes based on a dataset acquired at a parking lot of OSU (Retscher *et al.,* 2020).

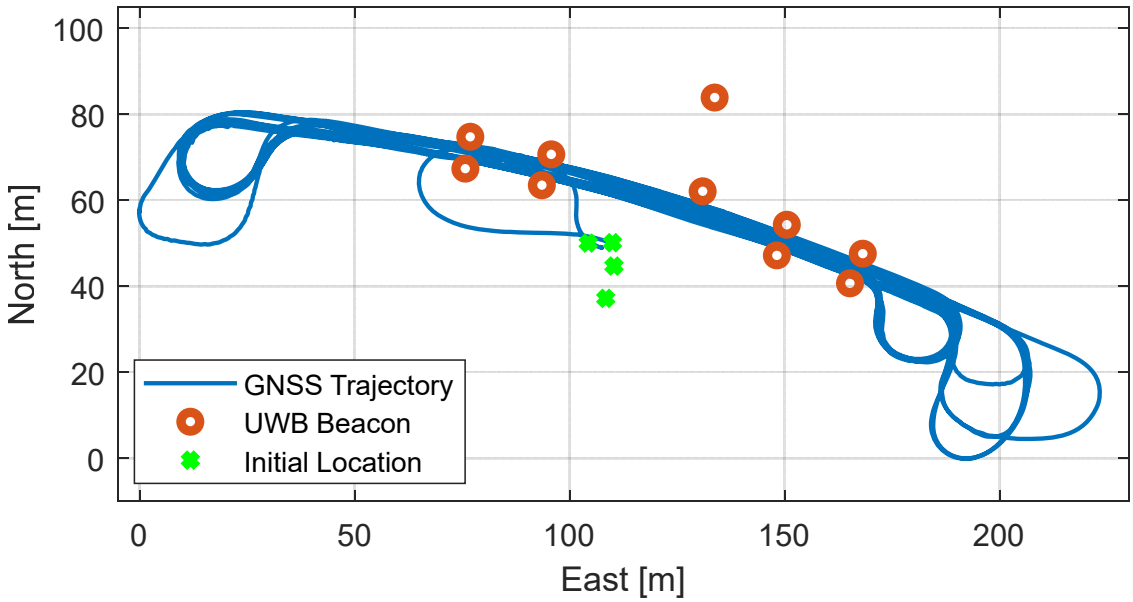

Figure 23 GNSS trajectory of GPSVan, UWB beacon locations, and the initial locations of the test vehicles.

From a typical test run, a period of 42.6 seconds, 214 epochs, of data was selected for this study. As the UWB measurement success rate was around 50%, V2V ranges were partially simulated from GNSS solutions with a standard deviation of 0.05 m. There were missing V2I ranges, which were also simulated at the same level of accuracy from the known locations of UWB beacons and vehicle A's GNSS solution.

The collaborative navigation results are depicted in Figure 24 and then used as reference for the test scenarios discussed below. Since the GNSS solutions are from standard point positioning, the differences between collaborative navigation and GNSS solutions are at sub-meter level as shown in Table 6 Statistics of differences between collaborative navigation and GNSS solution [m]..

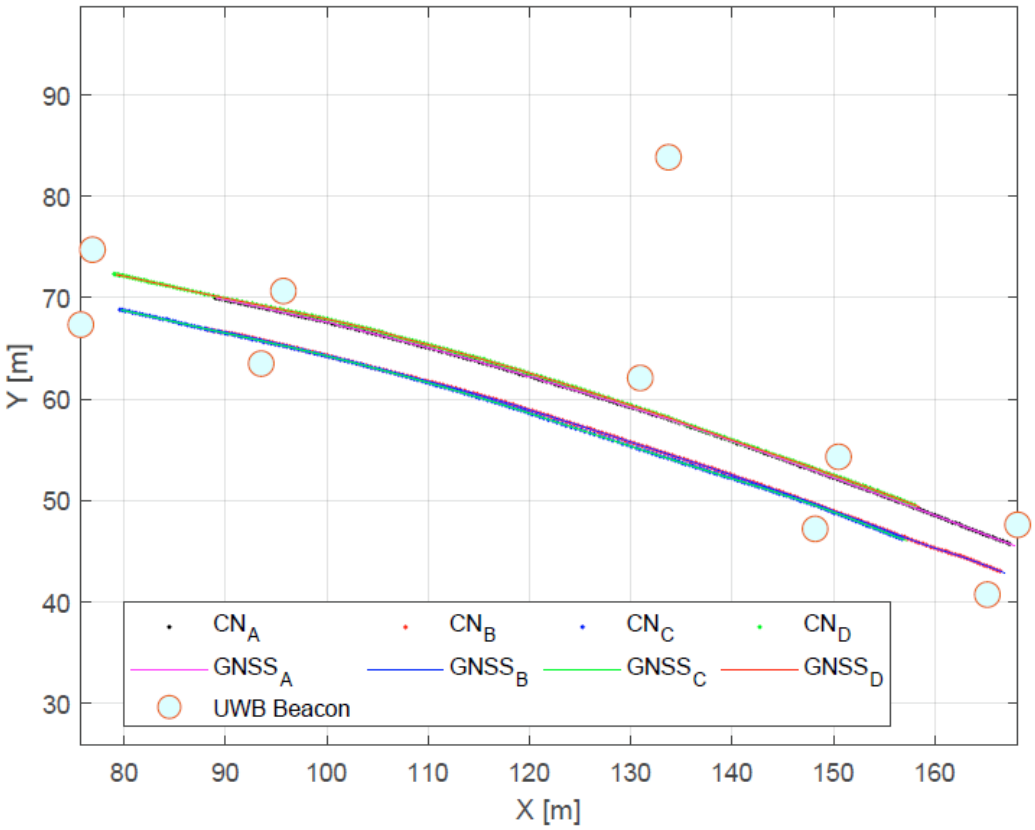

Figure 24 GNSS trajectory of GPSVan, UWB beacon locations, and the initial locations of the test vehicles.

Table 6 Statistics of differences between collaborative navigation and GNSS solution [m].

Vehicle	Min	Max	Mean	STD
A	0.01	0.07	0.06	0.07
B	0.01	0.26	0.06	0.06
C	0.02	0.18	0.06	0.06
D	0.01	0.15	0.06	0.07

To simulate a spoofing attack case like in (Rustamov *et al.,* 2020), a constant bias of 1.0 m was added to each component of vehicle D's GNSS solution starting from the 57th epoch for 100 epochs, and then it is used to derive the collaborative navigation with the other vehicles' GNSS solution as well as using V2I and V2V ranges. The reason to use 1 m bias was to address a challenging case, as detecting larger values is, obviously, easier in general. As seen from Figure 25 and Table 7 Statistics of differences between collaborative navigation for biased case and the reference solution [m]., using the information of other vehicles and the range measurements, the positioning error of vehicle D has been restricted to less than 0.2 m. After the bias-added periods, the solution gradually converged back to the reference solution. Obviously, any added biases larger than 1.0 m in GNSS solutions can be detected with precise inter-vehicle range measurements.

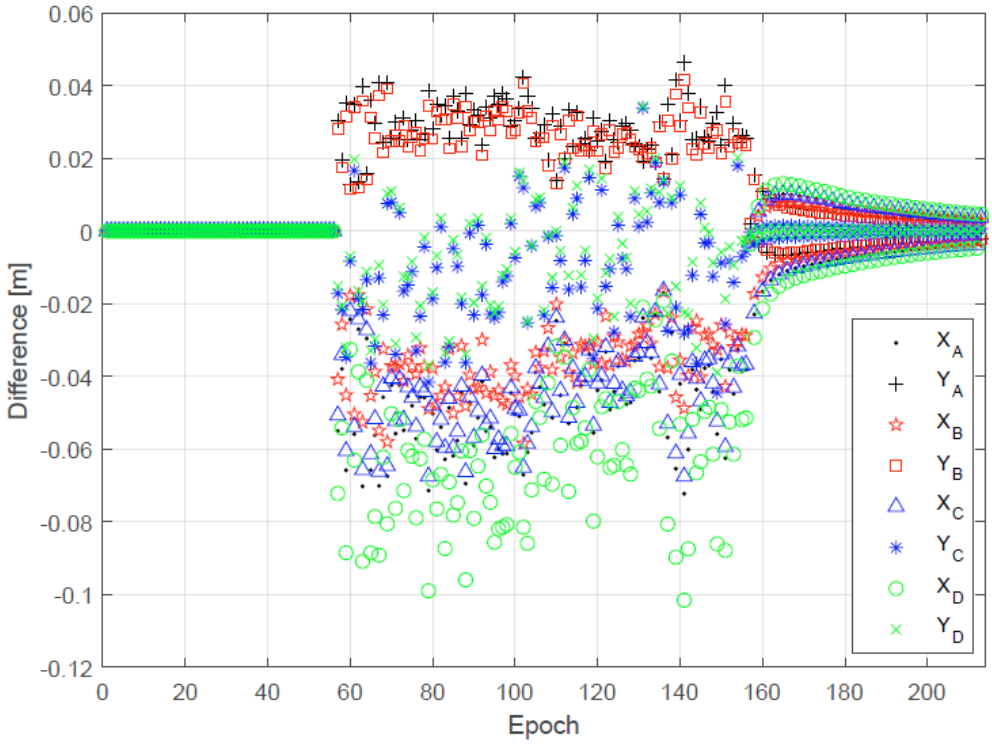

Figure 25 Differences between collaborative navigation for the biased case and reference solution.

Table 7 Statistics of differences between collaborative navigation for biased case and the reference solution [m].

Vehicle	Min	Max	Mean	STD
A	0.01	0.09	0.03	0.03
B	0.00	0.07	0.02	0.02
C	0.00	0.08	0.02	0.02
D	0.01	0.11	0.03	0.03

To investigate the situation that the GNSS receiver produces noisy positioning results due to interference, random noise with zero mean and variance of 1.0 m was added to each component of the GNSS solution of vehicle D. The collaborative navigation solution for this case is presented in Figure 26 and Table 8 Statistics of differences between collaborative navigation for noisy case and the reference solution [m].. Clearly, the collaborative navigation helps decrease the position error for vehicle D with the maximum 2D distance to the reference solution being below 0.5 m. Comparing to the result of the constant bias case above, however, the increased noise level creates challenges for detecting and mitigating GNSS anomalies.

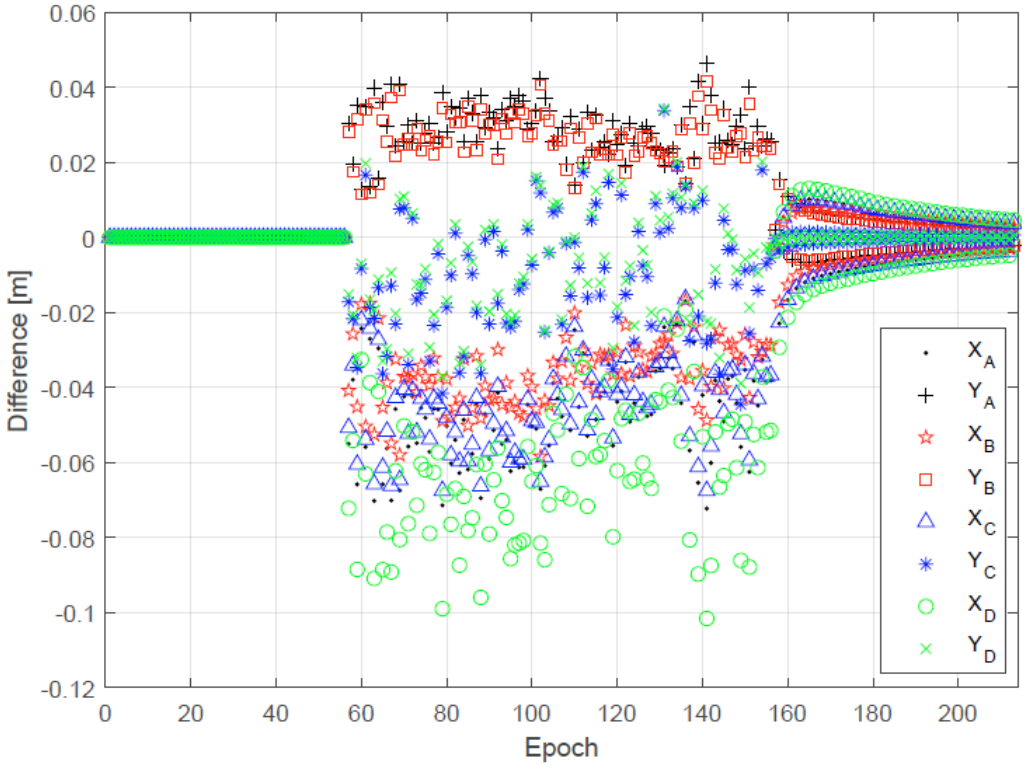

Figure 26 Differences between collaborative navigation for the noisy case and reference solution.

Table 8 Statistics of differences between collaborative navigation for noisy case and the reference solution [m].

Vehicle	Min	Max	Mean	STD
A	0.00	0.18	0.05	0.05
B	0.00	0.20	0.04	0.04
C	0.00	0.43	0.07	0.07
D	0.00	0.48	0.08	0.07

Note that decreasing the weight of D's GNSS solution for the whole duration of the affected periods before deriving the collaborative navigation, the offsets of D's solution can be limited to around 0.1 m. Obviously, techniques in the RF domain, such as C/N_0 monitoring and received power monitoring as in (Humphreys, 2017), should be combined to detect and mitigate the anomalies for this case.

In the presence of strong interference, most of the GNSS receivers may lose tracking of the satellite signals and produce no positioning results. There are some high-end, interference resistant GNSS receivers, however, that may still be able to position. This case is also investigated by assuming the GNSS solution is only available on vehicle A and then trying to derive the navigation solution for the other vehicles based on the V2V range measurements. The results are plotted in Figure 27 and tabulated in Table 9

Statistics of differences between collaborative navigation for single anchor case and the reference solution [m]., in which the differences to the reference solution are less than 1.2 m for B and 3.0 m for C and D; clearly demonstrating that the collaborative navigation can generate the navigation solution for the other three vehicles during the outage periods, which is rather unreal in single platform navigation without aiding from other sensors, such as IMUs and odometers/speedometers.

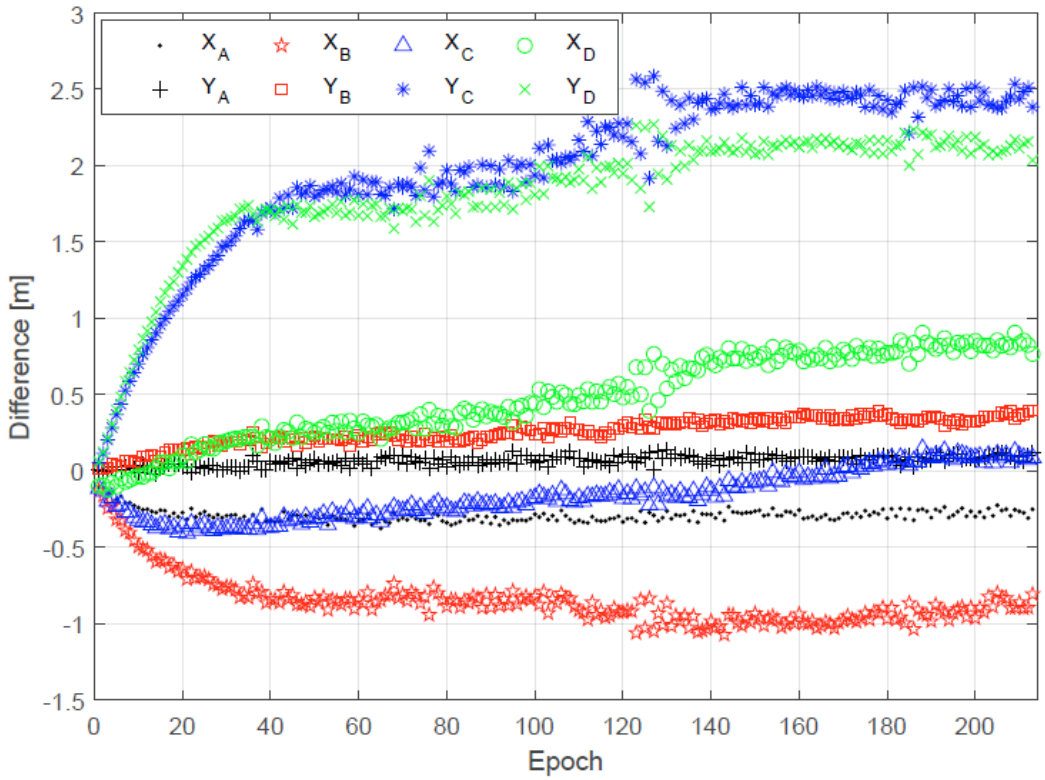

Figure 27 Differences between collaborative navigation for single anchor case and reference solution.

Table 9 Statistics of differences between collaborative navigation for single anchor case and the reference solution [m].

Vehicle	Min	Max	Mean	STD
A	0.10	0.39	0.30	0.04
B	0.13	0.12	0.89	0.17
C	0.14	2.59	2.00	0.52
D	0.11	2.40	1.89	0.45

Note that the solution differences seem to be larger than expected at first glance given the ranging accuracy of the V2V measurements. The reason for getting better results for vehicle B is that it was moving next to the side of vehicle A and thus could be positioned better. Vehicles C and D were behind the other two vehicles, and consequently were fairly well-positioned in the travel direction, while due to less favorable geometry their positioning in the lateral direction was noticeable less accurate. See the Y_c and Y_d vs X_c

and X_d Figure 27 and Table 9 Statistics of differences between collaborative navigation for single anchor case and the reference solution [m]. and consider that the vehicles moved approximately in the X direction.

Finally, it important to note that collaborative positioning in this case provides only relative positions, i.e., the solution is rotation invariant to vehicle A, and thus additional information is needed to orient the three vehicles' solution in the right direction.

4.6 Multiple outlier detection

The efficiency of detecting anomalies of individual PNT solutions in a collaborative navigation environment depends on the number of nodes in the network and the number of outliers vs good solutions. For example, for a three-node network, there must be two good solutions to detect the outlier solution. For larger networks, however, multiple outlier nodes can be detected too. We investigated the performance of detecting multiple outliers in PNT solutions in collaborative navigation using a combination of global test for outlier detection and the Akaike Information Criterion (AIC) method for outlier identification.

Multiple outlier detection is normally implemented as a consecutive execution of data snooping to detect one outlier at a time (Baarda, 1968). The process involves detection, identification, and rejection of single outliers (Lehmann and Losler; 2016) and down-weighting of the affected observations (Zhu *et al.,* 2020). A global test is normally taken to detect whether there are some outliers residing in the observations in a Gauss-Markov model (GMM) (Schaffrin, 1999). Under null hypothesis, the global test statistic can be formulated, which follows a $\chi 2$ distribution with a degree of observations minus number of adjusted parameters. When a threshold defined for a given probability is exceeded, the null hypothesis is rejected. The single outlier detection method can be extended into a multiple hypothesis test process which follows an *F* distribution (Schaffrin and Vang, 1994), and then based on the selected significance level, outliers are flagged. It is known that multiple outlier detection has swamping and masking side effects. The swamping effect tends to report more outliers than actually present, whereas multiple outliers can mask each other so that they are hardly detectable. Methods other than hypothesis test have been studied and applied for outlier detection (Lehmann and Losler, 2016).

A model selection criterion evaluates whether a fitted model achieves an optimal balance between fidelity to the data and model complexity among a candidate collection (Cavanaugh and Neath, 2019). Akaike Information Criterion (AIC), introduced in (Akaike, 1973), was the first model selection criterion and continues to be one of the most widely known and used model selection tools in statistical practice. The optimal fitting model is identified by the minimum values of AIC, which includes a goodness-of-fit term and a penalty term. When the sample size is large and the model dimension is relatively small, AIC is an asymptotically unbiased estimator of the expected Kullback discrepancy, a measure of similarity between the generating model of the data and a candidate model. For settings with small sample size and relatively large model dimension, AIC is substantially negatively biased, which leads to a further development of AIC, AICc (corrected AIC) with a refined penalty term (Cavanaugh and Neath, 2019).

Multiple outlier detection can be regarded as a problem of model selection on the null model free of outliers and different alternative models of outliers. Accordingly, AIC has been employed to detect multiple outliers in the scientific community (Kitagawa, 1979; Meloun et al., 2010; Cucina et al., 2014; Kornacki, 2014; Lehmann and Lösler, 2016). The benefits of using AIC to detect outliers are summarized as elegantly unifying the problems of determining the number of outliers and identifying the outliers, fitting various situations (single and multiple outliers, one-sided and two-sided outliers), requiring no input of significance level value, and avoiding masking effects.

4.7 Test results for the 2D case

A five-vehicle test dataset was used to study the performance of the AIC method for multiple outlier identification. The platforms had various sensor configuration. Vehicles A1, A2, and A3 had GNSS and tactical-grade IMU, then node B1 had GNSS and consumer-grade IMU, whereas node C1 had only consumer-grade IMU. The standard deviation of GNSS solution was 1.0 m, and the standard deviation of range measurements was 0.05 m. For simulations, the GNSS solution of A1 and A2 and the ranges between A3 and B1 were added with different bias levels to simulate various outlier scenarios. The details of the simulated outliers are listed in Table 10 Simulated outliers for the 2D dataset.; the indicator is used to identify the measurements. The evaluation used three methods for comparison:

- *AIC only:* The AIC method used for outlier detection and identification. The observations identified to have outliers are excluded from collaborative navigation.
- *Global test and AIC*: The global test in hypothesis test method is used to detect outliers, and AIC method is used to identify outliers. The observations identified to have outliers are excluded from collaborative navigation.
- *Outlier mitigation*: The global test and AIC method as above is used for outlier detection and identification. The observations identified to have outliers are corrected with the outlier estimates and then used in collaborative navigation.

Table 10 Simulated outliers for the 2D dataset.

Epoch	Measurements	Magnitude [m]	Indicator
131-190	GNSS (X, Y) of A1 Range of A3-B1	20 20	1 13
201-260	GNSS (X, Y) of A2 Range of A3-B1	10 15	2 13
271-300	GNSS (X, Y) of A1	12	1
341-400	GNSS (X, Y) of A2	10	2
411-470	GNSS (X, Y) of A1	8	1
481-540	GNSS (X, Y) of A2	6	2

The navigation results without any outlier detection are shown in Fig. 4.6. Not surprisingly, the mean errors of all nodes are around 4.0 m, and the maximum error can be as high as 15 m.

Outlier detection can also be implemented in the measurement update of the Kalman filter itself. The test statistics can be the Normalized Innovation Squared (NIS) as adopted in (Zhu et al., 2020). Figure 28 illustrates the NIS for this case, which has large values in outlier periods. With a carefully selected threshold, some outliers can be detected. Nevertheless, the identification of the outliers is still needed as the next step is to ultimately remove the effects of outliers.

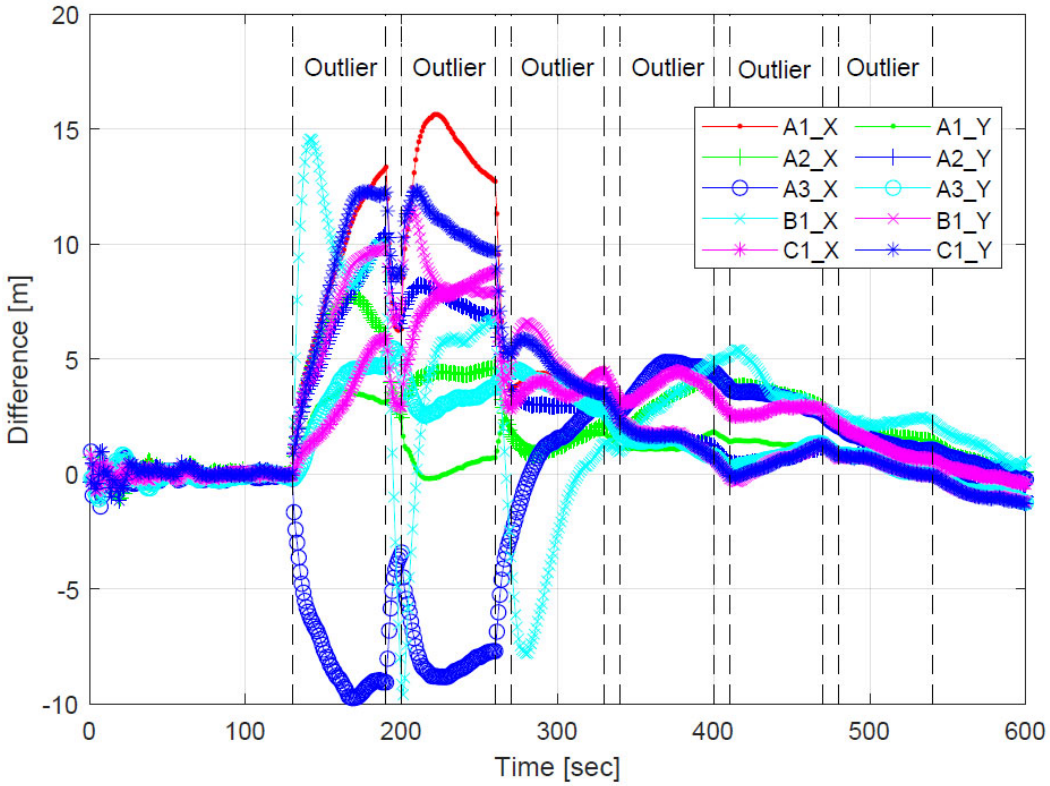

Figure 28 Positioning errors of collaborative navigation without outlier detection.

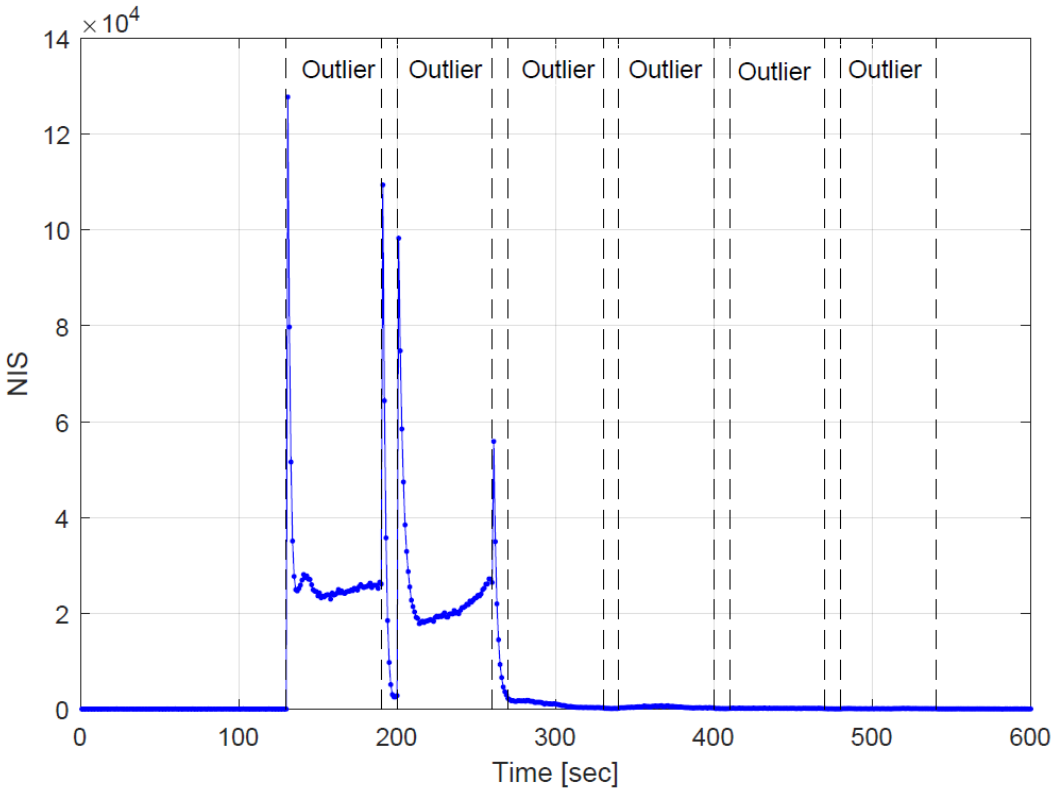

Figure 29 NIS of collaborative navigation without outlier detection.

Using the AIC method for outlier detection and identification, the AICc values are computed for the outlier free and alternative models with different outlier assumptions. The model that has the minimum AICc values is selected as the correct model. If the selected model is an alternative model, the observations that are suggested to have outliers are excluded from the collaborative navigation.

The collaborative navigation solution is shown in Figure 29. The identified outliers are depicted in Figure 30Figure 29. From these figures, it can be seen that outliers larger than 8.0 m are successfully detected and identified. Moreover, there is no single case of false positive error happening for the whole test. Especially for the first outlier period, both outliers GNSS and range are correctly detected and identified without input of the total number of outliers and the significance level of the hypothesis test. After the exclusion of the outliers, the mean errors of collaborative navigation have decreased from around 4.0 m to around 0.40 m. Interestingly, only 11 of 60 outliers at the 6 m level have been detected between epochs 481 and 540, the undetected outliers cause the collaborative navigation solution errors increase to 1.95 m by the end of the outlier periods.

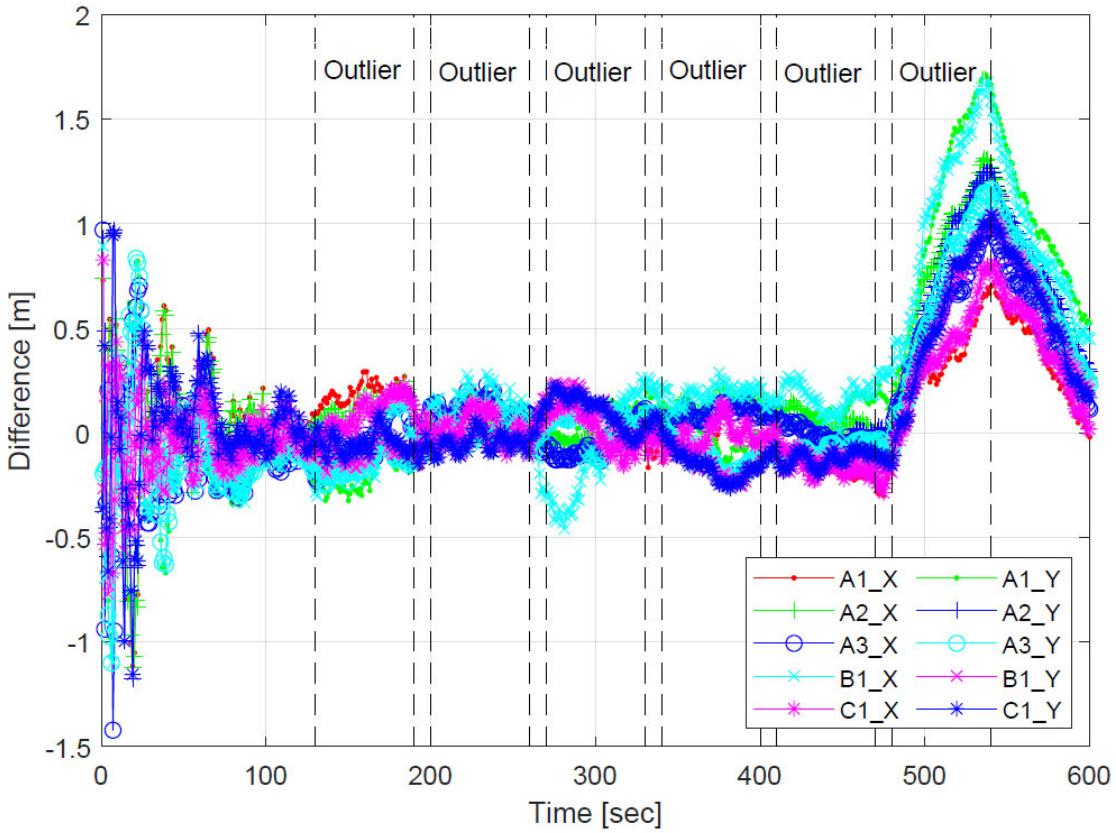

Figure 30 Positioning errors of collaborative navigation with AIC for outlier detection and identification.

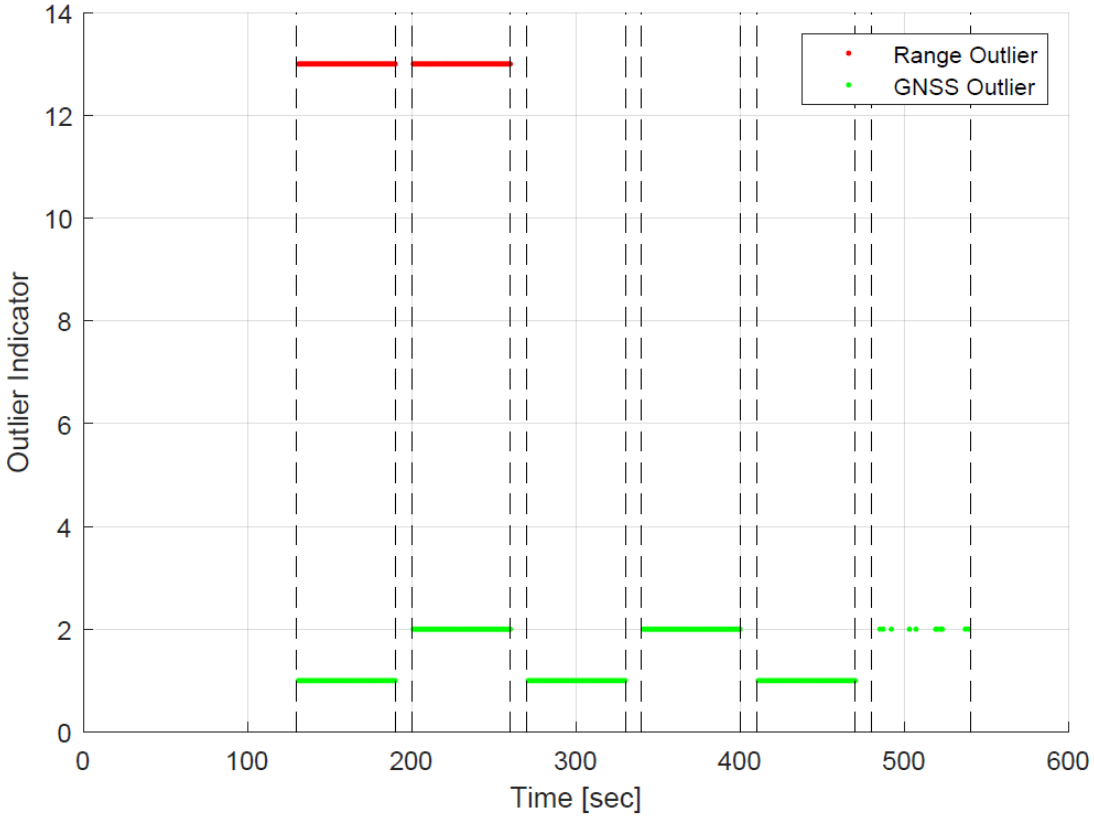

Figure 31 Identified outliers with the AIC method.

The presence of undetected outliers is also visible from the NIS plot in Figure 31. In the last outlier period, NIS values are generally two times of the values of the other periods, which demonstrates its value in outlier detection. However, outlier identification is still needed if NIS is used to detect outliers.

The logic to use the Global Test and AIC approach is that AIC cannot detect smaller outliers, as evidenced by the AIC only results above. A significance level of 0.01 was selected for the global test, and after the identification, the observations tested to have outliers are excluded from collaborative navigation.

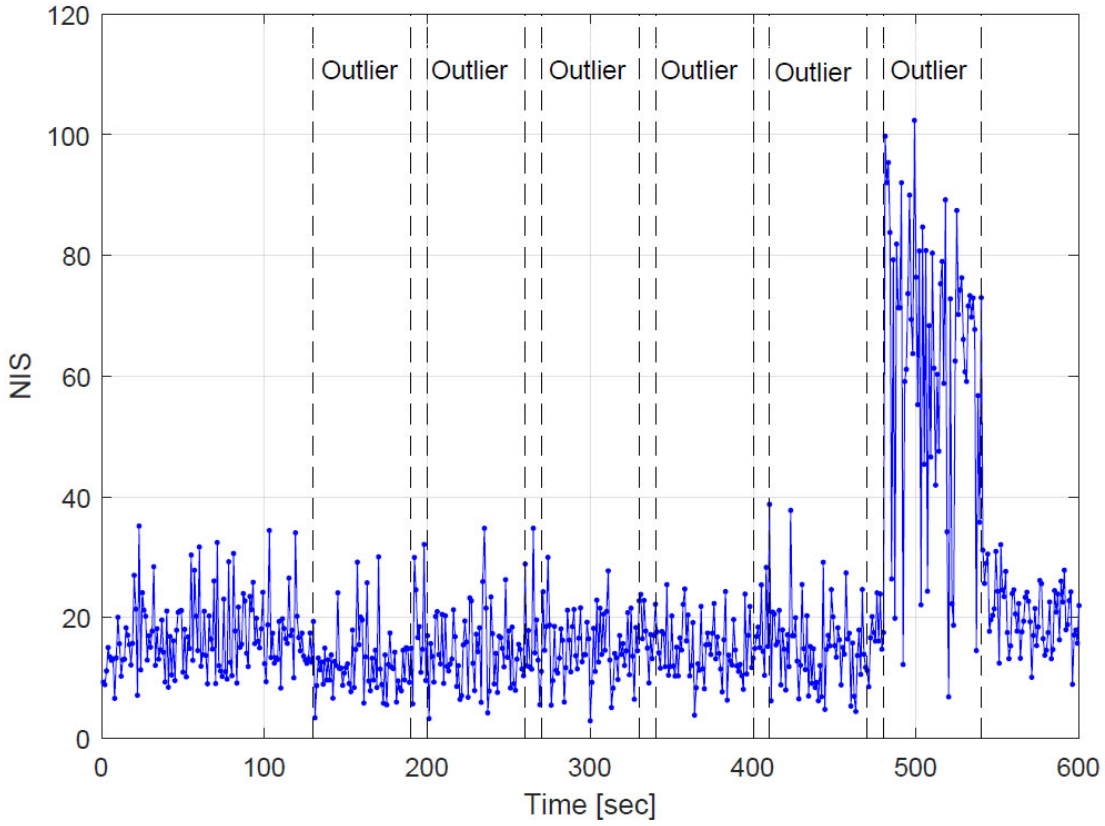

Figure 32 NIS of collaborative navigation with AIC for outlier detection.

The collaborative navigation solution errors are illustrated in Figure 32. With the outliers being detected and excluded, the mean errors have further decreased to around 0.20 m.

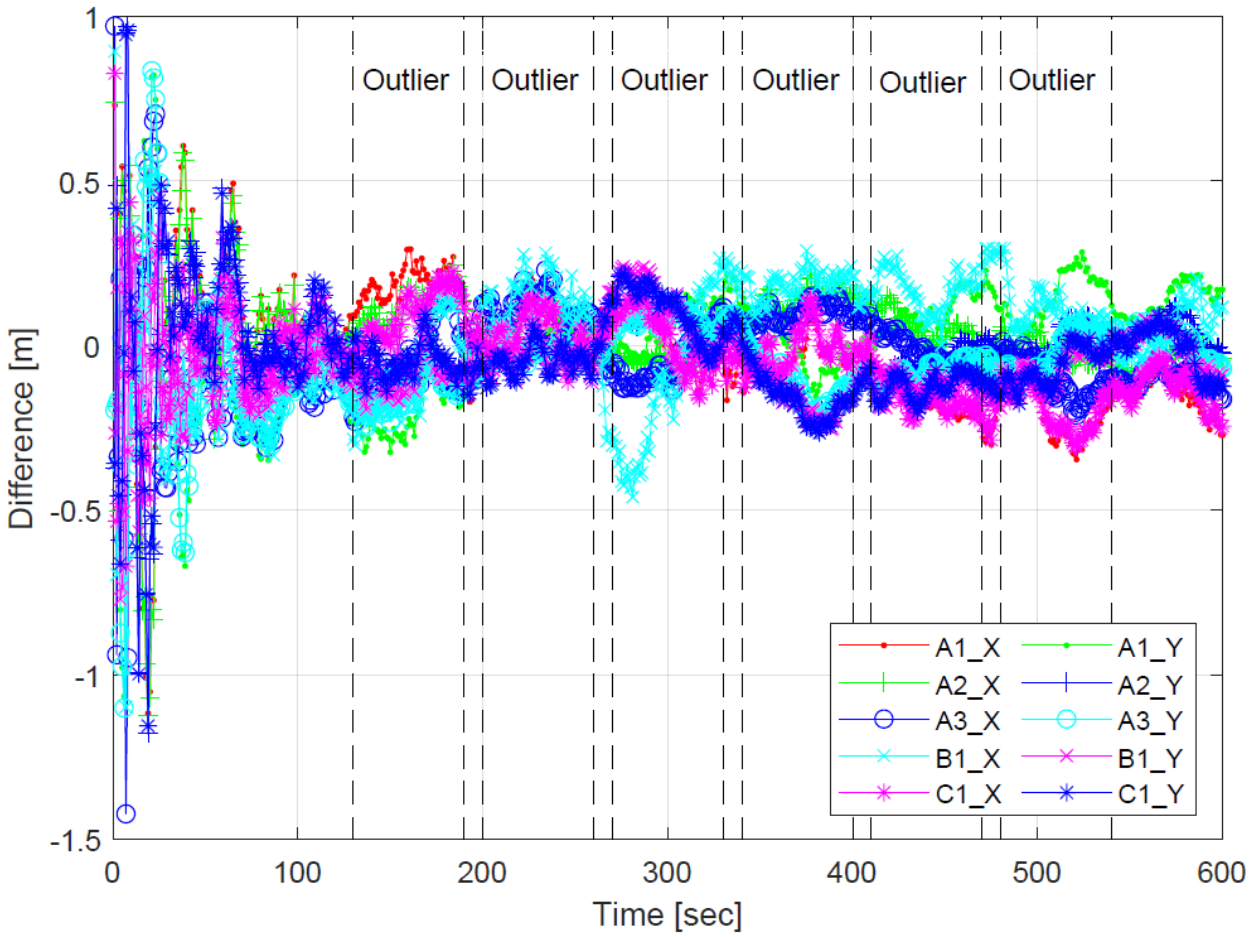

Figure 33 Positioning errors of collaborative navigation with combining global test and AIC for outlier detection and identification.

The detected outliers are shown in Figure 33, demonstrating that all outliers have been successfully detected and identified. Note that there is a single gap at epoch 512 where no outliers are detected. The missed detection can be cross checked with the NIS plot in Figure 34, in which a peak of 58 is present in the last outlier period. Utilizing the combined method has improved the outlier detection rate from 18.3% to 98.3% for the last outlier period.

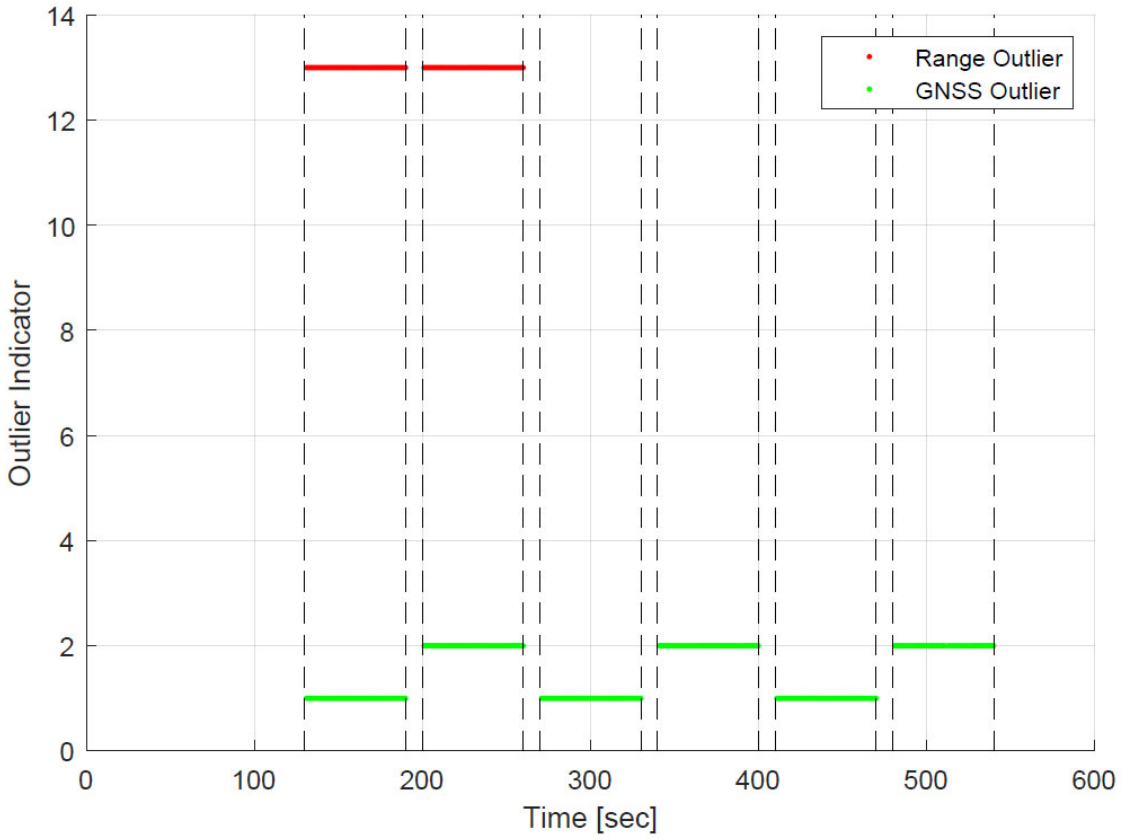

Figure 34 Identified outliers with the combining global test and AIC.

These results suggest that the global test method may have reached the Minimum Detectable Bias (MDB), 6.0 m in this case. Since the noise level of the GNSS solution is 1.0 m, the MDB of the hypothesis test can be roughly regarded as six times of the observation noise. The MDB by AIC seems to be larger than that of the hypothesis test. There are a few studies on MDB in hypothesis test, such as (Baarda, 1968; Schaffrin, 1997; Yang et al., 2013), yet further study is needed to determine the MDB of the AIC method, or a better method to calculate the AIC values.

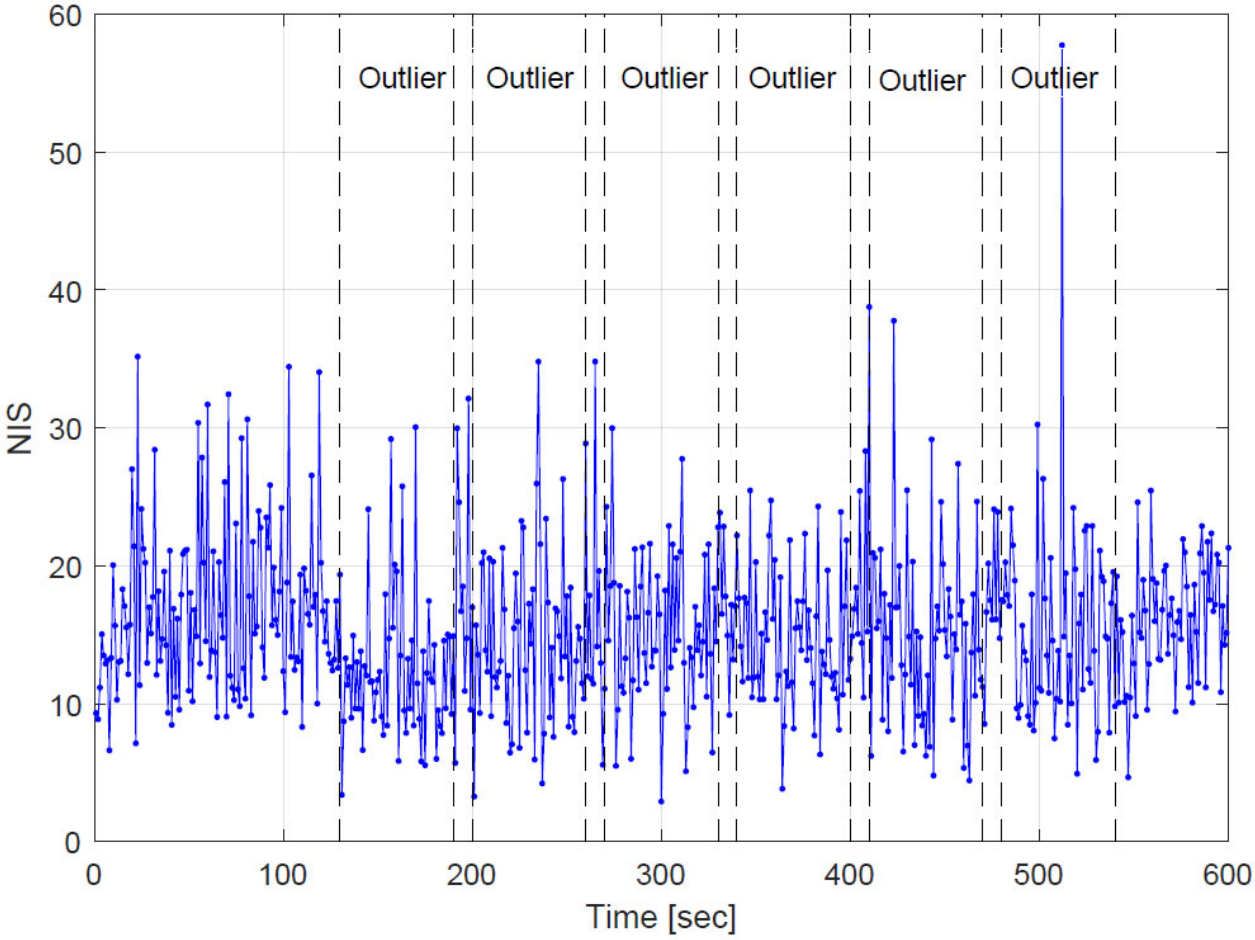

Figure 35 NIS of collaborative navigation with combining global test and AIC for outlier detection and identification.

4.8 Test results for the 3D case

From the May 2022 data acquisition, described earlier, an eight-platform dataset was extracted, including four cars (A, B, C, and D), two bicycles (E and F) and two drones (G and H). Figure 36 illustrates the reference trajectories of the test. All the processing and evaluation steps were similar to the 2D case discussed above. The simulated outliers scenarios are listed in Table 11 Simulated outliers for the 3D dataset..

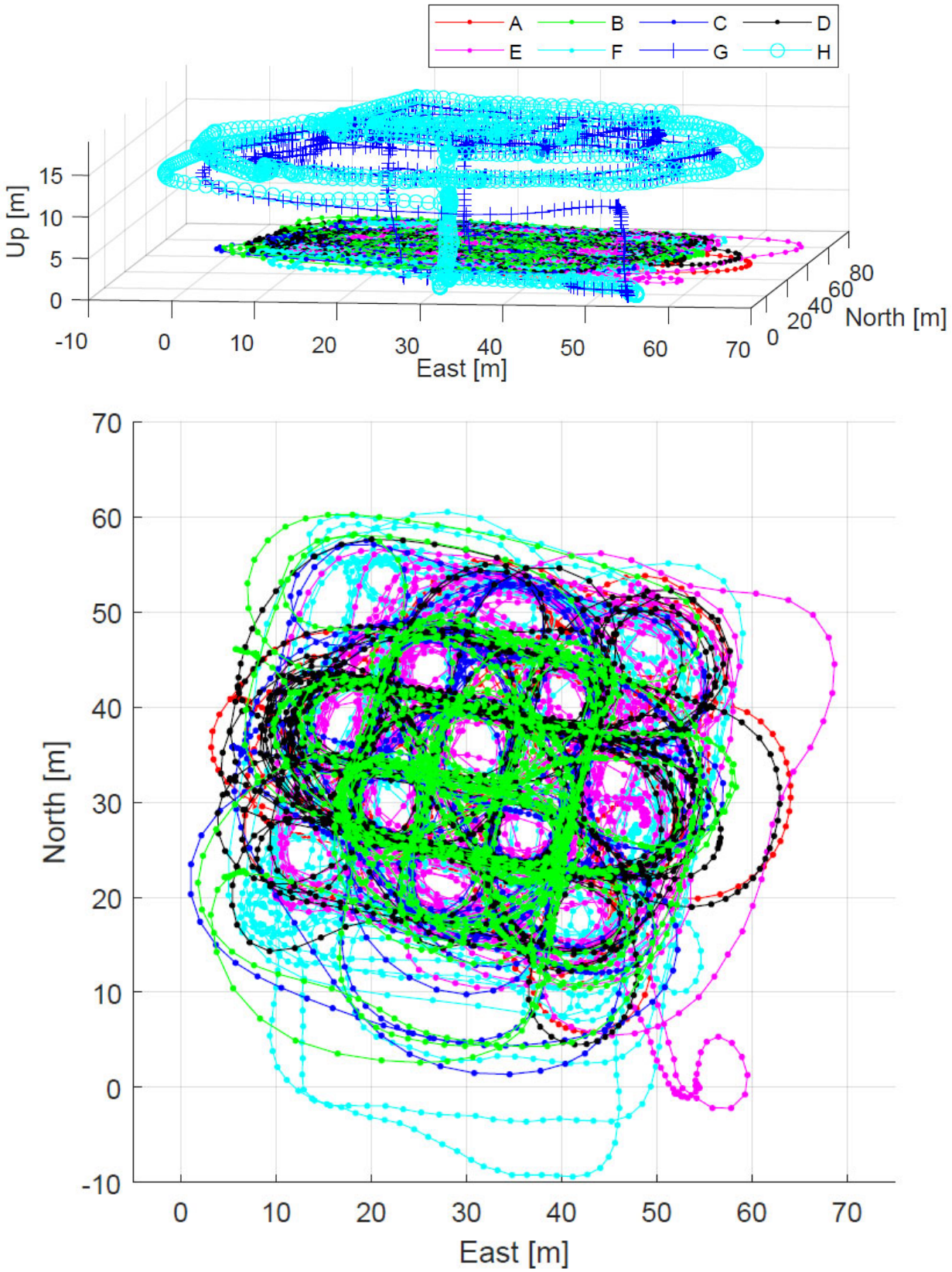

Figure 36 Reference trajectories used for simulated multiple outlier detection and identification.

Table 11 Simulated outliers for the 3D dataset.

Epoch	Measurements	Magnitude [m]	Indicator
101-200	GNSS (X, Y, Z) of A GNSS (X, Y, Z) of B Range C-D	10.0 10.0 10.0	s 2 22
301-400	GNSS (X, Y, Z) of B Range C-D	8.0 10.0	2 22
601-700	GNSS (X, Y, Z) of B	6.0	2
701-800	GNSS (X, Y, Z) of A	6.0	s
801-900	GNSS (X, Y, Z) of B	4.0	2
901-1000	GNSS (X, Y, Z) of A	4.0	s
1101-1200	GNSS (X, Y, Z) of B	2.0	2
2001-2100	GNSS (X, Y, Z) of A	2.0	s
2101-2200	GNSS (X, Y, Z) of B	1.0	2
2201-2300	GNSS (X, Y, Z) of A	1.0	s
2301-2400	GNSS (X, Y, Z) of B	0.3	2
2401-2500	GNSS (X, Y, Z) of A	0.3	s

The collaborative navigation solution errors are shown in Figure 37. Not surprisingly the maximum errors can be as high as 12 m for the outlier epochs, and the mean errors are around 1.2 m for vehicles A and B. In outlier free periods, the maximum and mean errors are less than 0.3 m and 0.1 m, respectively, for all platforms.

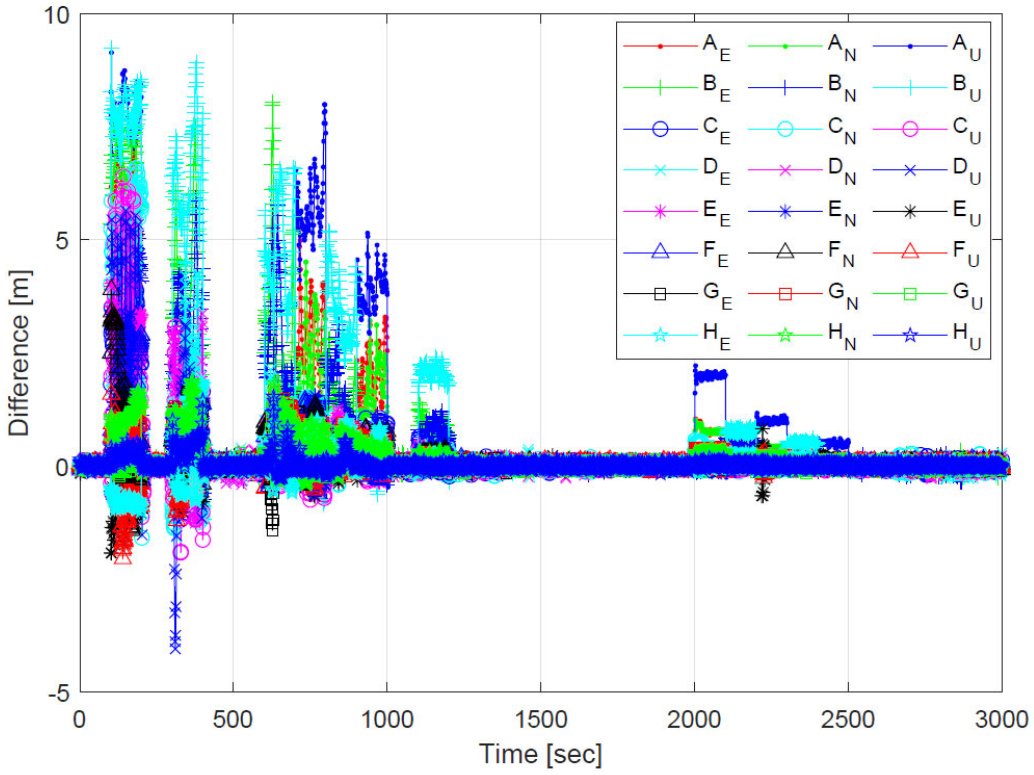

Figure 37 Positioning errors of collaborative navigation without outlier detection for a 3D dataset.

Using the combined global test and AIC method for outlier detection and identification, collaborative navigation solution errors are illustrated in Figure 38. The maximum and mean errors of B have been decreased to 2.88 m and 0.17 m, respectively. It is also apparent from Figure 38 that the maximum errors are mainly in the vertical direction, where the geometry is weak because six out of eight platforms are on the ground (obviously, the performance may be improved by integrating IMU measurements).

The outlier identification result is of more interest here. As depicted in Figure 39, the identified outliers confirm with Table 4.8 in terms of times and indicators. There are no false positive errors for the whole test. Most importantly, three simultaneous outliers in the first outlier period and two in the second have been successfully detected and identified, without a prior knowledge of how many outliers residing in the observations. In terms of sizes, outliers from 10.0 m to 0.5m have been correctly identified. As the observation noises are about 0.05 m, 0.5 m is ten times of the noise level, which confirms the assumption of six times of the observation noise as the MDB discussed above.

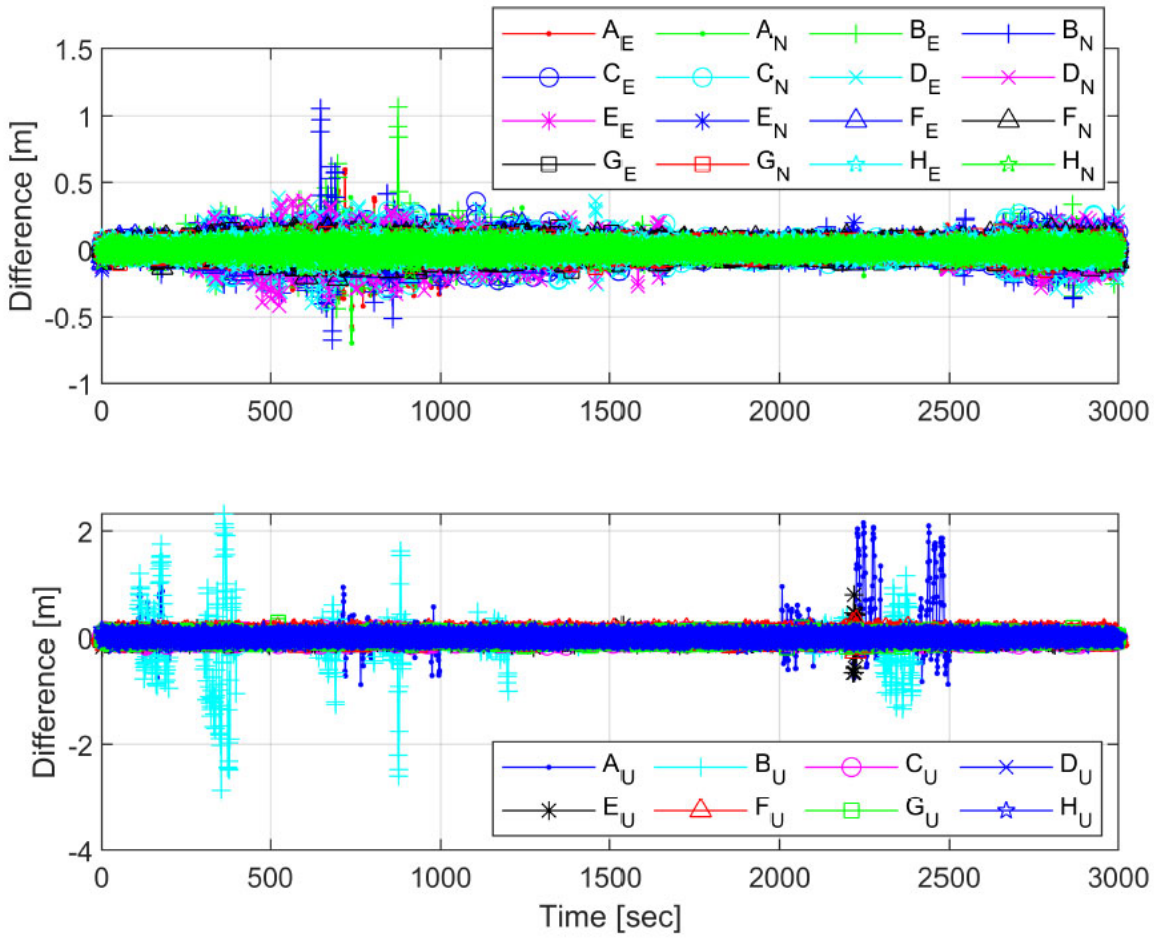

Figure 38 Positioning errors of collaborative navigation with combining global test and AIC.

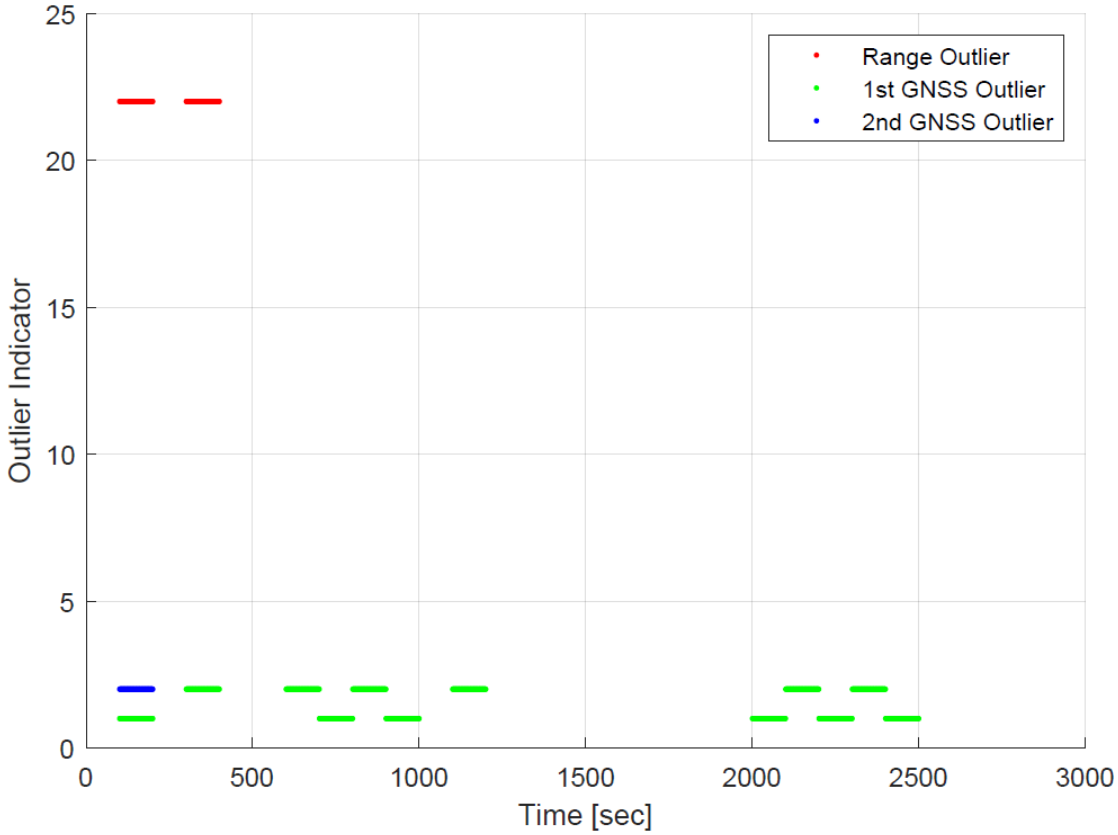

Figure 39 Identified outliers with combining global test and AIC.

Based on our test results on two datasets (2D and 3D) with known truths, the acclaimed attributes of effectiveness and simplicity of the AIC method can be confirmed. This method solves the problem of outlier detection and outlier identification all at once. Moreover, there is no need to assign a significance level and the total number of outliers in the detection procedure. For the tests on a 2D data set with observation noises of 1.0 m, all outliers larger than 6.0m have been successively detected and identified, including a set of two simultaneous GNSS and range outliers. Combining AIC with the global test offers further improvements in multiple outlier detection; in particular, detecting relatively smaller outliers.

5 References

5.1 Publications by CARMEN effort related to Section 2

1. Masiero, A., P. Dabove, L. Morelli, C. Toth, F. Remondino (2023), Benchmarking Collaborative Positioning and Navigation Between Ground and UAS Platforms, *Int. Arch. Photogramm. Remote Sens. Spatial Inf. Sci.*, under publishing, 2023
2. Masiero, A.; Toth, C.; Gabela, J.; Retscher, G.; Kealy, A.; Perakis, H.; Gikas, V.; Grejner-Brzezinska, D. Experimental Assessment of UWB and Vision-Based Car Cooperative Positioning System. *Remote Sens*. 2021, 13, 4858. https://doi.org/10.3390/rs13234858
3. Suleymanoglu, B., Toth, C., Masiero, A., and Ladai, A.: Monitoring the Environment in Smart Cities: The Importance of Geospatial Location Referencing, Int. Arch. Photogramm. *Remote Sens. Spatial Inf. Sci.*, XLVIII-M-1-2023, 355–360, https://doi.org/10.5194/isprs-archives-XLVIII-M-1-2023-355-2023, 2023.
4. Masiero, A., Toth, Ch., Remondino, F. (2023), Vision and UWB-Based Collaborative Positioning Between Ground and UAS Platforms, 2023 *IEEE/ION Position, Location and Navigation Symposium (PLANS)*, Monterey, CA, April 2023, pp. 748-754.
5. Masiero, A., P. Dabove, V. Di Pietra, M. Piragnolo, A. Vettore, A. Guarnieri, C. Toth, V. Gikas, H. Perakis, K.-W. Chiang, L. M. Ruotsalainen, S. Goel, and J. Gabela (2022), A Comparison Between UWB and Laser-Based Pedestrian Tracking, *Int. Arch. Photogramm. Remote Sens. Spatial Inf. Sci.*, XLIII-B2-2022-839-2022 https://doi.org/10.5194/isprs-archives-XLIII-B2-2022-839-2022
6. Ladai, A., C. Toth (2022), Range-based Network Formation to Support Georeferencing of Mapping Swarm Platforms, *Int. Arch. Photogramm. Remote Sens. Spatial Inf. Sci.*, XLVI-M-2-2022, 147–152, 2022, https://isprs-archives.copernicus.org/articles/XLVI-M-2-2022/147/2022/

5.2 Publications by CARMEN effort related to Section 3

7. Tenny, Robert, Humphreys, Todd E., "Robust Navigation for Urban Air Mobility via Tight Coupling of GNSS with Terrestrial Radionavigation and Inertial Sensing," Proceedings of the 35th International Technical Meeting of the Satellite Division of The Institute of Navigation (ION GNSS+ 2022), Denver, Colorado, September 2022, pp. 1599-1609. https://doi.org/10.33012/2022.18469

5.3 Publications by CARMEN effort related to Section 4

8. Xiankun Wang, Alternative Navigation Methods in GNSS Challenged Environments, Dissertation, OSU, 2023, (being published)
9. Wang, X., Ch. Toth, D. Grejner-Brzezinska, A. Masiero (2022), Collaborative Navigation: Supporting PNT System Operational Anomaly Detection, *IFAC-PapersOnLine*, Volume 55, Issue 24, 2022, Pages 285-291, https://doi.org/10.1016/j.ifacol.2022.10.298
10. Toth, Ch., D. Grejner-Brzezinska, X. Wang (2021), Between-Platforms Data Sharing to Support PNT Integrity Monitoring, Proceedings, ION GNSS+ 2021, September 20-24, 2021, St Louis, MO, pp.
11. Wang, X., Ch., Toth, D. Grejner-Brzezinska, (2021), Survey on Integrity Monitoring of GNSS Navigation for Ground Vehicles, Proceedings, ION GNSS+ 2021, September 20-24, 2021, St Louis, MO, pp.

5.4 Generic references

12. Akaike; H. (1973). "Information theory and an extension of the maximum likelihood principle." In: *2nd international symposium on information theory* (Budapest; Hungary; Sept. 2-8; 1971). Ed. by B. Petrov and F. Csaki, Akademiai Kiado; pp. 267-281.
13. Baarda, W. (1968). Testing Procedure for Use in Geodetic Networks. Tech. rep. Delft, The Netherlands: Netherlands Geodetic Commission.
14. Blanch, J., T. Walker, P. Enge, Y. Lee, B. Pervan, M. Rippl, A. Spletter, and V. Kropp (2013). "Baseline advanced RAIM user algorithm and possible improvements." In: *IEEE Transactions on Aerospace and Electronic Systems* 31.1, pp. 713-732.
15. Blanch, J., T. Walter, and P. Enge (2017). "Theoretical results on the optimal detec- tion statistics for autonomous integrity monitoring." In: *Navigation* 64.1, pp. 123- 137.
16. Blanch, J., K. Gunning, T. Walter, L. de Groot, and L. Norman (2019a). "Reducing Computational Load in Solution Separation for Kalman Filters and an Application to PPP Integrity." In: Proceedings of the 2019 International Technical Meeting of The Institute of Navigation (Reston, VA, Jan. 28-31, 2019), pp. 720-729.
17. Blanch, J., T. Walter, G. Berz, J. Burns, B. Clark, M. Joerger, M. Mabilleau, I. Martini, C. Milner, B. Pervan, and Y. Lee (2019b). "Development of advanced RAIM minimum operational performance standards." In: Proceedings of the 32nd International Technical Meeting of the Satellite Division of The Institute of Navigation (Miami, FL, Sept. 16-20, 2019), pp. 1381-1391.

18. Brown, R., and G. Chin (1997). "GPS RAIM: Calculation of threshold and protection radius using Chi-Square methods - A geometric approach." In: Global Positioning System Red Book Series 3, pp. 133-178.
19. Buehrer, R. M., Wymeersch, H., Vaghefi, R.M., 2018. Collaborative Sensor Network Localization: Algorithms and Practical Issues. Proc. IEEE, 106(6), pp. 1089-1114.
20. Cavanaugh, J. and A. Neath (2019). "The Akaike information criterion: Background, derivation, properties, application, interpretation, and refinements." In: *WIREs Computational Statistics* 11.3, e1460.
21. Cucina, D., A. di Salvatore, and M. K. Protopapas (2014). "Outliers detection in multivariate time series using genetic algorithms." In: *Chemometrics and Intelligent Laboratory Systems* 132, pp. 103-110.
22. Humphreys, T., “Interference,” in Springer *Handbook of Global Navigation Satellite Systems*, P. Teunissen and O. Montenbruch. Ed. Springer. 2017, pp. 469-504.
23. Joerger, M., F. Chan, and B. Pervan (2014). "Solution separation versus residual-based RAIM." In: *Navigation* 61.4, pp. 273-291.
24. Kitagawa, G. (1979). "On the use of AIC for the detection of outliers." In: *Technometrics* 21.2, pp. 193-199.
25. Kornacki, A. (2014). "Application of the Akaike criterion to detect outliers for the analysis of ash content in barley straw." In: *International Agrophysics* 28.2.
26. Lee, J., Grejner-Brzezinska, D., Toth, C., 2012. Network-based Collaborative Navigation in GPS-Denied Environment. *The Journal of Navigation*, Vol. 63(3), pp. 443-437.
27. Lee, Y. (1986). "Analysis of range and position comparison methods as a means to provide GPS integrity in the user receiver." In: Proceedings of the 42nd Annual Meeting of The Institute of Navigation (Seattle, WA), pp. s-4.
28. Lehmann; R. and M. Losler 2016). "Multiple Outlier Detection: Hypothesis versus Model Selection by Information Criteria." In: *Journal of Surveying Engineering* 142.4; p. 04016017.
29. Maaref, M., J. Khalife, and Z. Kassas (2018). "Integrity monitoring of LTE signals of opportunity-based navigation for autonomous ground vehicles." In: Proceedings of the 31st International Technical Meeting of the Satellite Division of The Institute of Navigation (Miami, FL, Sept. 24-28, 2018), pp. 2436-2466.
30. Meloun, M., S. Bordovska, and K. Kupka (2010). "Outliers detection in the statistical accuracy test of a pKa prediction." In: *Journal of Mathematical Chemistry* 47.2, pp. 891-909.
31. El-Mowafy, A., B. Xu, and L. Hsu (2020). "Integrity monitoring using multi-GNSS pseudorange observations in the urban environment combining ARAIM and 3D city models." In: *Journal of Spatial Science*. 20 pp.
32. Retscher, G., Kealy, A., Gabela, J., Li, Y., Goel, S., Toth, C., Masiero, A., Blaszczak-Bak, W., Gikas, V., Perakis, H., Koppanyi, Z., and Grejner-Brzezinska, D. (2020). A benchmarking measurement campaign in gnss-denied/challenged

indoor/outdoor and transitional environments. *Journal of Applied Geodesy*, 14(2), 215–229. doi:https://doi.org/10.1515/jag-2019-0031.

33. A. Rustamov, N. Gogoi, A. Minetto, and F. Dovis, “Assessment of the vulnerability to spoofing attacks of GNSS receivers integrated in consumer devices,” in 2020 International Conference on Localization and GNSS (ICL-GNSS), Tampere, Finland, June 2-4, 2020, 6 pp.
34. Schaffrin, B. and Z. Wang (1994). "Multiplicative outlier search using homBLUP and an equivalence theorem.' In: *Manuscripta Geodaetica* 1994.20, pp. 21-26.
35. Schalfrin, B. (1997). "Reliability Measures for Correlated Observations." In: *Journal of Surveying Engineering* 123.3, pp. 126-137.
36. Schaffrin, B. (1999). "Softly unbiased estimation, part 1: The Gauss-Markov model." In: *Linear Algebra and its Applications* 289.1, pp. 285-296.
37. Temple, T. (2006). "Autonomous error bounding of position estimates from GPS and Galileo." MA thesis. MIT.
38. Wang, S. and Jiang, X., 2021. Three-Dimensional Cooperative Positioning in Vehicular Ad-hoc Networks. *IEEE Transactions on Intelligent Transportation Systems*, Vol. 22(2), pp. 937-930.
39. Yang, L., J. Wang, N. Knight, and Y. Shen (2013). "Outlier separability analysis with a multiple alternative hypotheses test." In: *Journal of Geodesy* 87.6, pp. 391-604.
40. Yang, Y. and J. Xu (2016). "GNSS receiver autonomous integrity monitoring (RAIM) algorithm based on robust estimation." In: *Geodesy and Geodynamics* 7.2, pp. 117- 123.
41. Zhu, N., J. Marais, D. Betaille, and M. Berbineau (2018). "GNSS position integrity in urban environments: a review of literature." In: *IEEE Transactions on Intelligent Transportation Systems* 19.9, pp. 2762-2778.
42. Zhu, N., D. Betaille, J. Marais, and M. Berbineau (2020). "GNSS Integrity Monitoring Schemes for Terrestrial Applications in Harsh Signal Environments." In: *IEEE Intelligent Transportation Systems Magazine* 12.3, pp. 81-91.